Interactions between PAMAM dendrimers and DOPC lipid multilayers: Membrane thinning and structural disorder

Laura J. Fox [a,b], Anna Slastanova [b], Nicolas Taylor [b], Magdalena Wlodek [c], Oier Bikondoa [d,e], Robert M. Richardson [f] and Wuge H. Briscoe [b*]

a Bristol Centre for Functional Nanomaterials, H. H. Wills Physics Laboratory, University of Bristol, Tyndall Avenue, Bristol BS8 1TL, UK

b School of Chemistry, University of Bristol, Cantock's Close, Bristol BS8 1TS, UK

c Jerzy Haber Institute of Catalysis and Surface Chemistry, Polish Academy of Sciences, Niezapominajek 8, PL-30239 Krakow, Poland

d XMaS, The UK-CRG Beamline, The European Synchrotron (ESRF), 71 Avenue des Martyrs, 38043 Grenoble, France

e Department of Physics, University of Warwick, Gibbet Hill Road, Coventry CV4 7AL, UK

f School of Physics, H. H. Wills Physics Laboratory, University of Bristol, Tyndall Avenue, Bristol BS8 1TL, UK

*Email: wuge.briscoe@bristol.ac.uk, Tel: +44 (0)117 3318256

Graphical Abstract

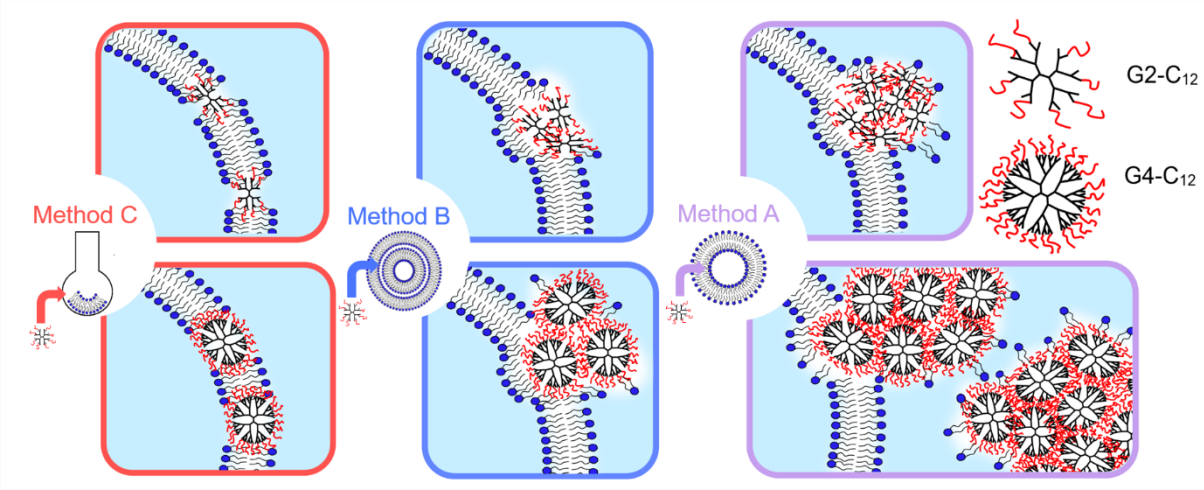

Abstract

Background

Understanding the structure of hybrid nanoparticle-lipid multilayers is of fundamental importance to their bioanalytical applications and nanotoxicity, where nanoparticle-membrane interactions play an important role. Poly(amidoamine) (PAMAM) dendrimers are branched polymeric nanoparticles with potential biomedical applications due to precise tunability of their physicochemical properties. Here, the effect of PAMAM dendrimers (2.9 - 4.5 nm) with either a hydrophilic amine (NH_2) or a hydrophobic C_{12} chain surface termination on the 1,2-dioleoyl-sn-glycero-3-phosphocholine (DOPC) multilayers has been studied for the first time.

Methods

DOPC multilayers were created by the liposome-rupture method *via* drop-casting dendrimer-liposome dispersions with the dendrimers added at different concentrations and at three different stages. The multilayer structure was evaluated *via* the analysis of the synchrotron X-ray reflectivity (XRR) curves, obtaining the bilayer *d*-spacing, the coherence length from the Scherrer (L_s) analysis of the Bragg peaks, and the paracrystalline disorder parameter (g).

Results

Dendrimer addition led to lipid bilayer thinning and more disordered multilayer structures. Larger hydrophobic dendrimers caused greater structural disruption to the multilayers compared to the smaller dendrimers. The smallest, positively charged dendrimers at its highest concentration caused the most pronounced bilayer thinning. The dendrimer-liposome mixing method also affected the multilayer structure due to different dendrimer aggregation involved.

Conclusions

These results show the complexity of the effect of dendrimer physicochemical properties and the addition method of dendrimers on the structure of mixed dendrimer-DOPC multilayers.

General significance

These insights are useful for fundamental understanding of nanotoxicity and future biomedical application of nanocomposite multilayer materials in which nanoparticles are added for enhanced properties and functionality.

Keywords: Nanoparticle-membrane hybrids; PAMAM dendrimers; Lipid multilayers; Nanotoxicity; Model membranes; Nanoparticle-membrane interactions; X-ray reflectivity

1. Introduction

Poly(amidoamine) (PAMAM) dendrimers are branched polymeric nanoparticles (NPs) with a range of potential biomedical applications due to precise tunability of their physicochemical properties [1]. They are comprised of layers (or *generations, G*) of branching units called dendrons radiating from a central core [2]. This branched structure results in interior cavities and an exponential increase in the number of terminal amine groups with increasing generation or dendrimer size [3]. In particular, dendrimers are being developed as vectors for drug [4] and gene delivery [5] due to several favourable characteristics including their ability to pass through the cellular membrane into the cytosol or lysosomes [6, 7], to complex with DNA *via* their terminal amine groups [8], and to solubilise hydrophobic drugs in their cavities [9]. PAMAM dendrimers can be functionalised in a variety of ways, most commonly with hydroxyl-termination, acetylation, or conjugation to hydrophobic chains [10]. However, due to the current gap in our knowledge of the relationship between the physicochemical properties of dendrimers and the cytotoxic response they elicit, the application of dendrimers in biomedicine remains to be fully exploited.

It has been previously reported that PAMAM dendrimers could cause disruption to plasma and lysosomal membranes during cell entry (*endocytosis*), which would then instigate programmed cell death (*apoptosis*). This cytotoxic effect has been shown to be related to dendrimer generation, charge, surface functionality, dosage, incubation time, and cell type [7, 11-16]. The large number of factors affecting dendrimer cellular uptake and trafficking, and different cell-specific endocytosis routes, have led to conflicting conclusions regarding the mechanism of dendrimer toxicity from multiple studies [17]. The *in vitro* uptake mechanism of amine terminated G4 (~ 4.5 nm in size) and G6 (~ 6.7 nm) PAMAM dendrimers by HaCaT (human keratinocytes) cells has been found to depend on the cellular entrance route [16]. Antibacterial studies [12, 13] found that PAMAM dendrimer toxicity to bacteria was dependant on its size, dose, and degree of PEGylation as well as the bacteria membrane composition (i.e. gram positive or negative).

Model membrane systems, such as small and large unilamellar (SUVs/LUVs) [18] or multilamellar vesicles (MLVs) [19-21], Langmuir-Blodgett (LB) monolayers [22, 23], supported lipid bilayers (SLBs) [18, 24-27], mesophases [28-30], purple membrane multilayers [31, 32], and computational models [33-35] have also been used to study membrane interactions. The interactions between dendrimers and model membranes have been probed using different methods, such as atomic force microscopy (AFM) [36], cryogenic transmission electron microscopy (cryo-TEM) [37], differential scanning calorimetry (DSC) [38], LB-trough [39], quartz crystal microbalance with dissipation monitoring (QCM-D) [40], neutron reflectivity (NR) [40], dye release assays [19], and molecular dynamics (MD) simulations [33, 41], as reviewed elsewhere [42, 43]. These studies show that the extent of dendrimer-membrane interactions and their impact depend on a number of factors, such as dendrimer size, concentration, surface chemistry, as well as the model membrane composition and elasticity.

For instance, amine-terminated dendrimers have been found to cause the removal of lipids from SLBs, forming nanoscale holes and resulting in cell lysis, as explored using AFM [36]. NR experiments [40] revealed that G6 PAMAM dendrimers disrupted the ordering of negatively charged POPG/POPC (1-palmitoyl-2-oleoyl-sn-glycero-3-phosphocholine/ 1-palmitoyl-2-oleoyl-sn-glycero-3-phosphocholine) SLBs but not neutral POPC SLBs, highlighting the importance of the membrane composition. G2-8 (2.9 – 9.7 nm) dendrimers have been found to induce vesicle aggregation, leading to vesicle disruption, an effect that was also dependent on the membrane phosphatidylethanolamine (PE) content [44]. In addition, disruption to LUVs was more pronounced than SUVs, attributed to larger LUV deformations upon aggregation. Furthermore, disruption of negatively charged 1-Palmitoyl-2-oleoyl-sn-glycero-3-phosphoethanolamine/ 1-palmitoyl-2-oleoyl-sn-glycero-3-phosphatidic acid (POPE/POPA) vesicles by G4-7 (4.5–8.1 nm) dendrimers was reported to depend on the dendrimer dosage [19].

Stacked membrane multilayers are also found in nature, such as myelin sheaths in nerves [45], and they also have applications in macroscale drug delivery [46], gene delivery [47], biocatalysis [48] and as artificial cell substrates [49]. Therefore, understanding their interactions with NPs are important for their future application in nanocomposite materials. Lipid multilayers have been conventionally prepared *via* spin casting lipids dissolved in organic solvents. It has been recently shown that stacked lipid bilayers (or multilayers) could be prepared by drop casting aqueous liposome dispersions on mica followed by drying [50], as characterised using X-ray reflectivity (XRR) with a 'bending mica' method [50-53]. Such a simple method makes it possible to incorporate water soluble or dispersible additives and nanofluids [54, 55] (such as dendrimers) into the multilayers. These lipid multilayers composed from phospholipids can also be used as a structural analogue of a cell membrane.

Here, we have studied the interactions between PAMAM dendrimers and lipid multilayers prepared using the drop-casting method. Hydrophilic amine and hydrophobic C_{12} chain terminated G2 and G4 PAMAM dendrimers have been added to 1,2-dioleoyl-sn-glycero-3-phosphocholine (DOPC) multilayers, prepared using three different methods. The change in the structural characteristics of the multilayers with incorporated PAMAM dendrimers of different size (or generation), surface chemistry, and dosage has been studied with XRR, giving insight into how the physicochemical properties of dendrimers influence their interactions with lipid bilayers. Our findings are of relevance to the fundamental understanding of cellular uptake and cytotoxicity of PAMAM dendrimers and demonstrate a method for the incorporation of functional NP additives in composite multilayer materials.

2. Materials and methods

2.1 Materials

1,2-dioleoyl-sn-glycero-3-phosphocholine (DOPC) (>99% purity, M_w = 786.113 g.mol^{-1}) in chloroform ($CHCl_3$, 25 mg.ml^{-1}) was purchased from Avanti® Polar Lipids, Alabaster, Alabama. Amine (NH_2)-terminated G2 (20 w%) and G4 (24 w%) and 50% C_{12} chain-terminated G2 (40.29

w%) and G4 (26.85 w%) PAMAM dendrimers dispersed in methanol were purchased from Dendritech, Inc., Midland, Michigan. They are referred to herein as G2-C_{12}, G4-C_{12}, G2-NH_2, and G4-NH_2 respectively. The hydrodynamic diameter of the dendrimers was measured using dynamic light scattering (DLS, Malvern Nano Zetasizer ZS), listed in

Table 1. Ultrapure Milli-Q (Merck Millipore) water (with a resistivity of 18.2 MΩ.cm^{-1} and total organic content (ToC) of 3-4 ppb) and nitrogen (Air Liquide, oxygen free) were used for sample preparation. Mica sheets were hand-cleaved and then cut to 3 cm × 1 cm in size and ~300 µm in thickness, as required for the 'bending mica' method [50, 51].

Table 1. Characteristics of G2 and G4 PAMAM dendrimers as described by manufacturer Dendritech, Inc.. a. DLS size data measured in methanol by us. b. Aggregates of up to several µm in size were observed with some measurements, with an example DLS curve shown in Figure S8 in SM. c. Aggregates of ~340 nm in size were observed with some measurements.

	G2 NH_2	G2 50% C_{12}	G4 NH_2	G4 50% C_{12}
Dendrimer	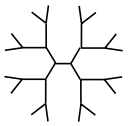	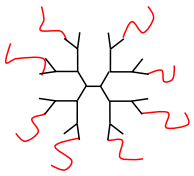	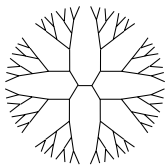	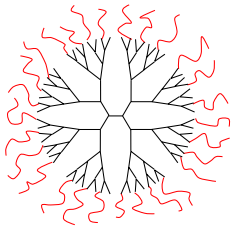
Terminal Group No.	16	16 (8 C_{12} chains)	64	64 (32 C_{12} chains)
MW (Da)	3256.18	6205	14214.17	26010
Manufacturer Diameter (nm)	2.9	-	4.5	-
DLS Diameter[a] (nm)	2.1-2.3	2.8-3.3[b]	3.8[c]	7.1

2.2 Preparation of DOPC liposomes and multilayers

DOPC liposomes were prepared by the extrusion method and DOPC multilayers were prepared by drop-casting the liposomes, as reported by Sironi *et al.* [50]. Briefly, DOPC in $CHCL_3$ (25 mg.mL^{-1}) was measured into a 7 mL glass vial and the $CHCl_3$ was evaporated at room temperature using gentle nitrogen flow, followed by drying for ~1 h in a vacuum oven (Heraeus Vacutherm VT 6025) at ~1 mbar to form a uniform lipid film. The film was then hydrated to a concentration of 2 mg·mL^{-1} using Milli-Q water and sonicated (Ultrawave QS5) for 1 h to form multi-lamellar vesicles (MLVs). The MLV suspension was then extruded using a LIPEX™ 10 mL Thermobarrel Extruder at room temperature (Northern Lipids Inc., Burnaby, Canada) 5 times with a 200 nm pore-sized polycarbonate membrane (Whatman® Nuclepore™ Track-Etched Membranes) and 10 times with a 100 nm membrane using ~20 bar pressure of N_2 to create small unilamellar vesicles (SUVs).

The size distribution and polydispersity (PDI) of liposome dispersions were determined by DLS and the results are collected in Table S1 in Supplementary Materials (SM). SUVs were ~75 nm in diameter (PDI 0.2). As expected, the unextruded MLVs were polydisperse, as the vesicles form onion like structures of varying sizes before being extruded through a polycarbonate membrane[56]. After extrusion to SUVs the PDI decreased. A PDI of <0.3 for liposomes is generally accepted as indicating a homogenous population [57]. The PDI and average liposome diameter increased, on average, with increasing number ratio of dendrimers to lipids, ν. Further discussion on liposome aggregation can be found in Section S3, SM.

2.3 Dendrimer addition to liposome dispersions

A schematic of three methods used to add the dendrimers to DOPC liposome dispersions is presented in Figure 1. G2-C_{12} and G4-C_{12} dendrimers were dispersed in Milli-Q water and added to DOPC SUVs (**Method A**) or to DOPC MLVs before extrusion (**Method B**). Alternatively, they were dispersed in methanol and added to the DOPC-chloroform suspension (**Method C**). The concentrations of G2-C_{12} and G4-C_{12} dendrimers added using Methods A, B and C were 0.01, 0.1 and 2 mg·mL^{-1}, respectively, which corresponded to dendrimer lipid number ratios ν = 0.00015, 0.0015 and 0.03 for G4-C_{12} dendrimers and ν = 0.00063, 0.0063 and 0.127 for G2-C_{12} dendrimers. G2-NH_2 and G4-NH_2 were mixed with DOPC-chloroform dispersions to create liposomes using **Method C** only, in dendrimer-lipid number ratios ν = 0.02 and 0.2.

2.4 DOPC multilayers with incorporated dendrimers

100 µl of the dendrimer-liposome dispersions, and pure G4-C_{12} dispersion in Milli-Q (4 mg·mL^{-1}) were drop-cast on freshly cleaved mica and left to dry in a vacuum oven at ~1 mbar and at room temperature for ~ 18 h. The multilayers were kept in sealed vials at 4°C for up to 7 days until XRR measurements. For clarity, we denote the mixed DOPC-dendrimer multilayers samples as DOPC-Gi-f(ν)A/B/C, where i = 2, 4 for the two dendrimer generations, f = C_{12} or NH_2 for the dendrimer functionalisation, ν is the dendrimer-lipid number ratio and A/B/C represents the mixing method. For example, DOPC-G2-NH_2(0.2)C denotes a 0.2 number ratio of amine (NH_2) terminated G2 dendrimers to DOPC lipids, mixed using method C, used to make a multilayer.

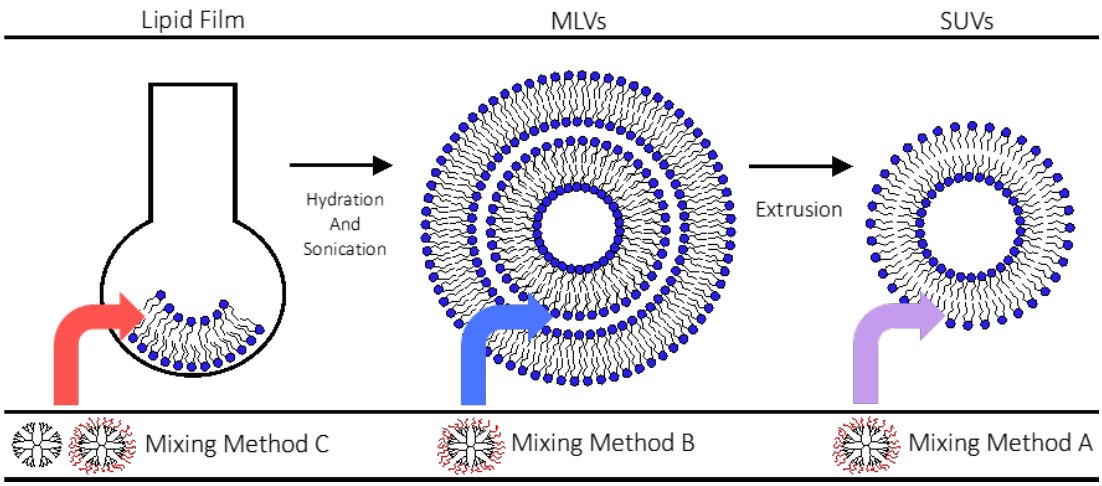

Figure 1. Schematic of addition/incorporation of PAMAM dendrimers at the different stages of liposome preparation. G2-C_{12} and G2-C_{12} were added using the three methods, whilst G2-NH_2 and G4-NH_2 Method C only.

2.5 X-ray reflectivity measurements and data analysis

XRR measurements were undertaken at the XMaS beamline (BM28) at the ESRF in Grenoble. The mica substrate with the multilayers was mounted on a curved stage inside of a liquid cell as shown in Figure 2b. Two attached heating plates allowed the cell to be heated to 40 °C (Figure 2a). The beam energy used was 14 keV and the specularly reflected intensity was detected at each angle using an avalanche photodiode detector (APD). To correct for the beam footprint, a 'spline' fit of a fine scan taken along the *z*-axis (at incident angle $\vartheta_i = 0$) was used to generate a Gaussian model of the beam.

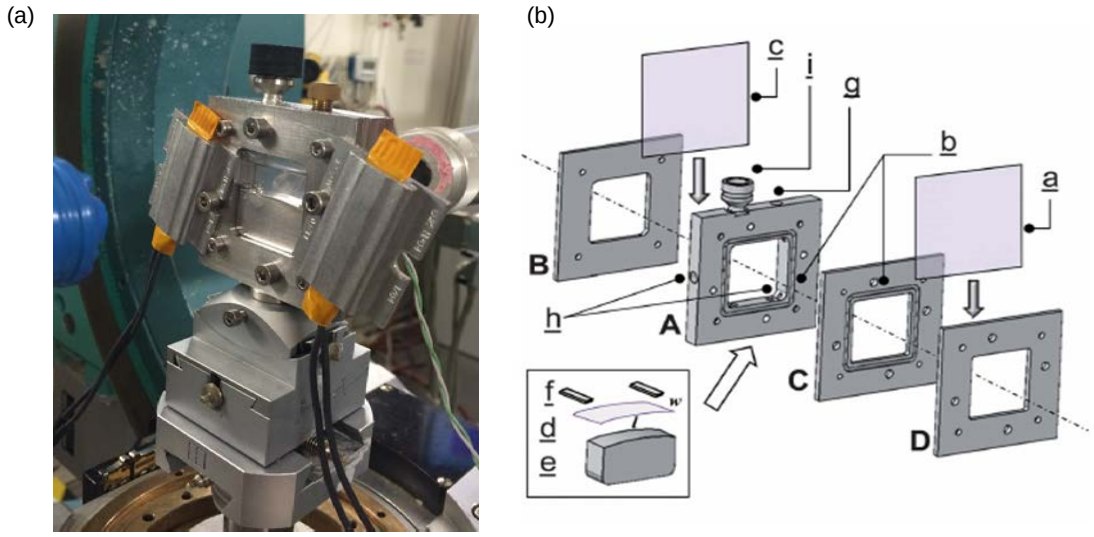

Figure 2. (a) Mica liquid cell mounted at ESRF BM28. (b) Schematic of the liquid cell used for XRR measurements. Four stainless steel plates (A – D) compose the shell of the cell enclosing the core (d – f). A cleaved mica sheet (d) is clamped through two small plates (f) onto the mica cylindrical support (radius = 7 cm) (e), which is inserted between plate A and C. Two Mylar

sheets (a, c) are inserted respectively between plates A – B and C – D. Plates A and B and plates C and D are clamped together, Viton® O-rings placed in grooves (b) facilitate the sealing and prevent leaking. A system of inlet/outlet (g, h) allows gas exchange. An inlet nozzle (i) on top of plate A allows in situ injection of liquid samples and solvents. Heating plates were also attached to the outer plates for measurements at 40 °C. Reproduced with permission from Briscoe *et al*. [51]

The specularly reflected intensity (i.e. reflection angle ϑ_r = incident angle $\vartheta_i = \vartheta$) was collected as a function of ϑ_i and the obtained reflectivity was plotted against momentum transfer Q [Å^{-1}] normal to the interface, where $Q = \frac{4\pi}{\lambda} sin\left(\frac{2\theta}{2}\right)$ with $\lambda = 0.89$ Å the wavelength of the incident X-ray beam. In the case of multilayers on the surface, Bragg peaks were observed and the lattice or *d*-spacing (or bilayer thickness) in the multilayer can be calculated using,

$$d = \frac{2\pi h}{Q_h} \qquad (1)$$

where Q_h is the position of the Bragg peak of order h. The ratio of the peak positions is characteristic of the crystalline phase of the structure. For lipid multilayers, the Bragg peaks were equally spaced (h = 1,2,3…) indicating that the phase was lamellar.

In some cases, multiple peaks (n = 0, 1, 2,…) in the same order (h) were resolved due to bilayer thickness fluctuations or polymorphism, which revealed the complex structure of the sample. The full width at half maximum (FWHM), ΔQ_{hn}, of these resolved peaks was used to obtain further structural information such as the paracrystalline disorder, *g,* which is a measure of the lattice or *d*-spacing fluctuations. Peak width or broadening is determined by the natural linewidth of the X-rays, instrumental effects and sample effects including the crystallite size and strain.

Coherence length, L, is the lower limit of the crystalline domain size perpendicular to the mica surface (along the direction of the Q vector and can be determined using the Scherrer equation (labelled as L_s) or from the peak broadening (labelled as L_b). The coherence length L_s , is obtained using the Scherrer equation [58, 59],

$$L_s = \frac{2\pi K}{\Delta Q_{hn}} \qquad (2)$$

where K is the Scherrer or shape constant and depends upon the crystal shape and is approximately of order unity. L_s can be used as an indicator of the structural order of the multilayers. The instrumental effects on peak broadening were constant as the same set-up was used throughout.

The paracrystalline disorder, g, was derived from a plot of the broadening of complementary peaks, $\frac{\Delta Q_{hn}{}^2}{2\pi^2}$, vs. the fourth power of the diffraction order, h^4, for a plane of Miller index (h00), where h = 1, 2, 3, 4 and n is constant. g was derived from the gradient m of a linear fit ($y = y_0 + mh^4$) to this plot and the coherence length L_b was derived from the intercept y_0 using,

$$L_b = y_0^{-\frac{1}{2}} \qquad (3)$$

$$g = \frac{(md^2)^{\frac{1}{4}}}{\pi} \qquad (4)$$

Calculation of g and L_b using this method requires each reflection properly resolved and background scatter subtracted. The disordered nature of the multilayers in our system meant that the errors associated with L_b were large, and we thus did not pursue this analysis for L_b. Instead, we performed the Scherrer analysis to the well-defined 1st Bragg peaks (h = 1). The number of bilayers m in the domain can then be estimated as $= \frac{L_s}{d}$.

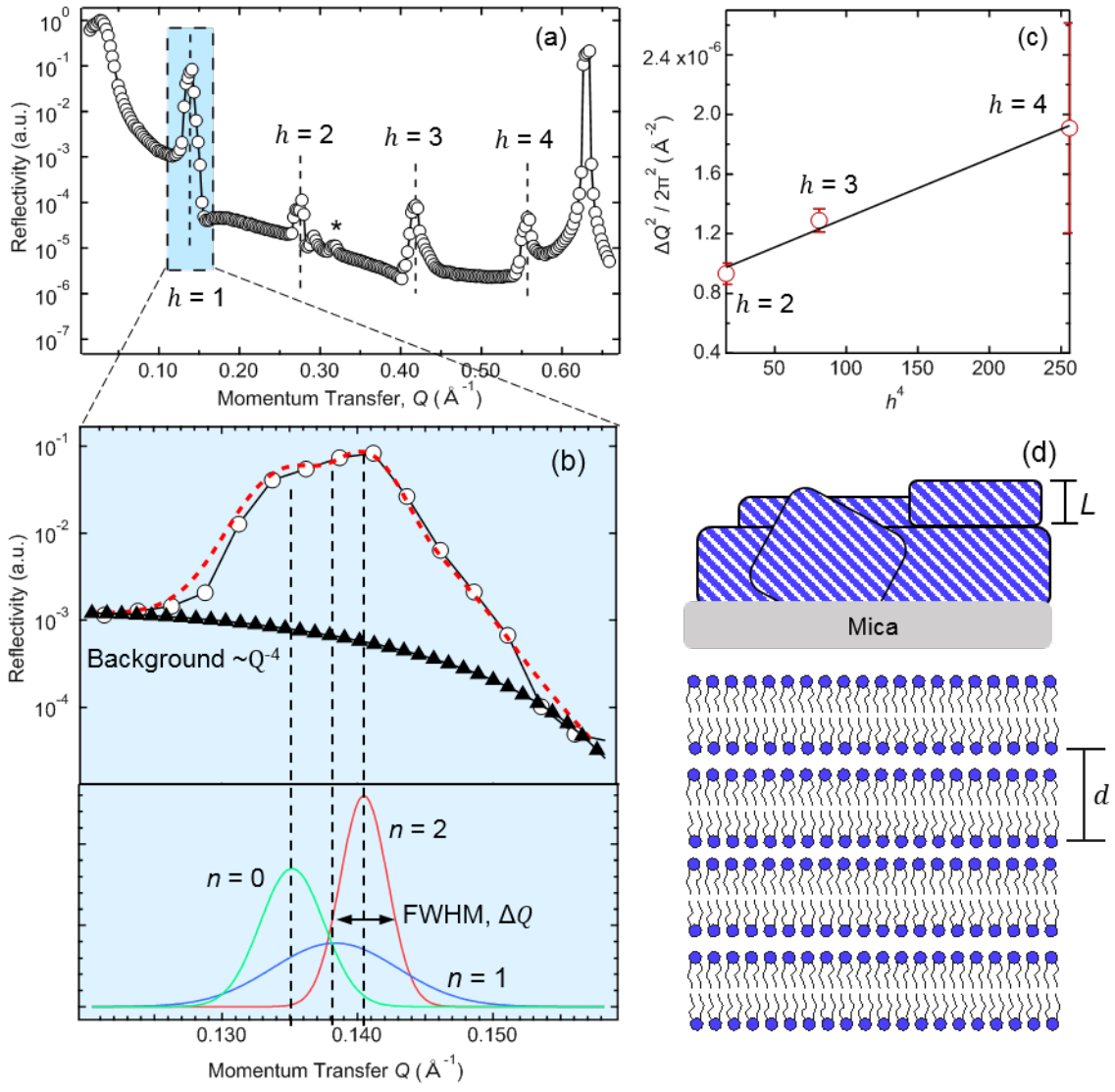

Figure 3. (a) Example experimental XRR curve for DOPC-G2-C_{12}(0.127)A on mica at room temperature. The Bragg peak observed at Q = 0.63 Å is from the mica substrate. The forbidden half-Bragg of mica is marked with an asterisk (*) and the Bragg peaks associated with the multilayer structure are labelled with their reflection order (h = 1, 2, 3, and 4). (b) An enlarged view of the reflectivity on a log-linear scale around the first order (h = 1) Bragg Peak with the

background fitted to Q^{-4} (triangles) and the fit (dashed line) calculated with IGOR Pro 'Multi-Peak' Fit operations. The fitted peak could be decomposed into three Gaussian peaks indicating polymorphism (n = 0,1,2). (c) A plot of peak broadening $\Delta Q^2/2\pi^2$ vs. the fourth power of the diffraction order h^4 with linear fit for h = 2, 3 and 4 (complementary peak, n, for h = 1 could not be resolved). (d) Schematic showing multilayers on mica, the coherence length, L and the lamellar repeat distance or d-spacing.

3. Results and discussion

We describe in detail in the SM (Section S4) the results from the DOPC multilayers without any dendrimers and from drop-cast dendrimer layers – both as control, facilitating a comparison with the dendrimer-loaded DOPC multilayers.

3.1 Bilayer thinning and structural disorder: Effect of mixing method and dendrimer size

The reflectivity profiles of DOPC-G4-C_{12}(0.03) multilayers with the larger G4-C_{12} dendrimers from all three mixing methods (*cf.* Figure 1; Lipid film, MLVs, and SUVs) are shown in Figure 4iii-iv. Overall, compared to the pure DOPC SUV multilayer XRR curve (Fig.4i) the dendrimer addition altered the positions and the FWHM of the Bragg peaks, indicative of structural changes in the multilayers. The average d-spacing, the coherence length L_s and the paracrystalline disorder parameter g are listed in Table S2 in SM. Polymorphism was observed in all the DOPC-G4-C_{12} samples, with all the resolvable peaks also listed (*cf*. Table S5, SM).

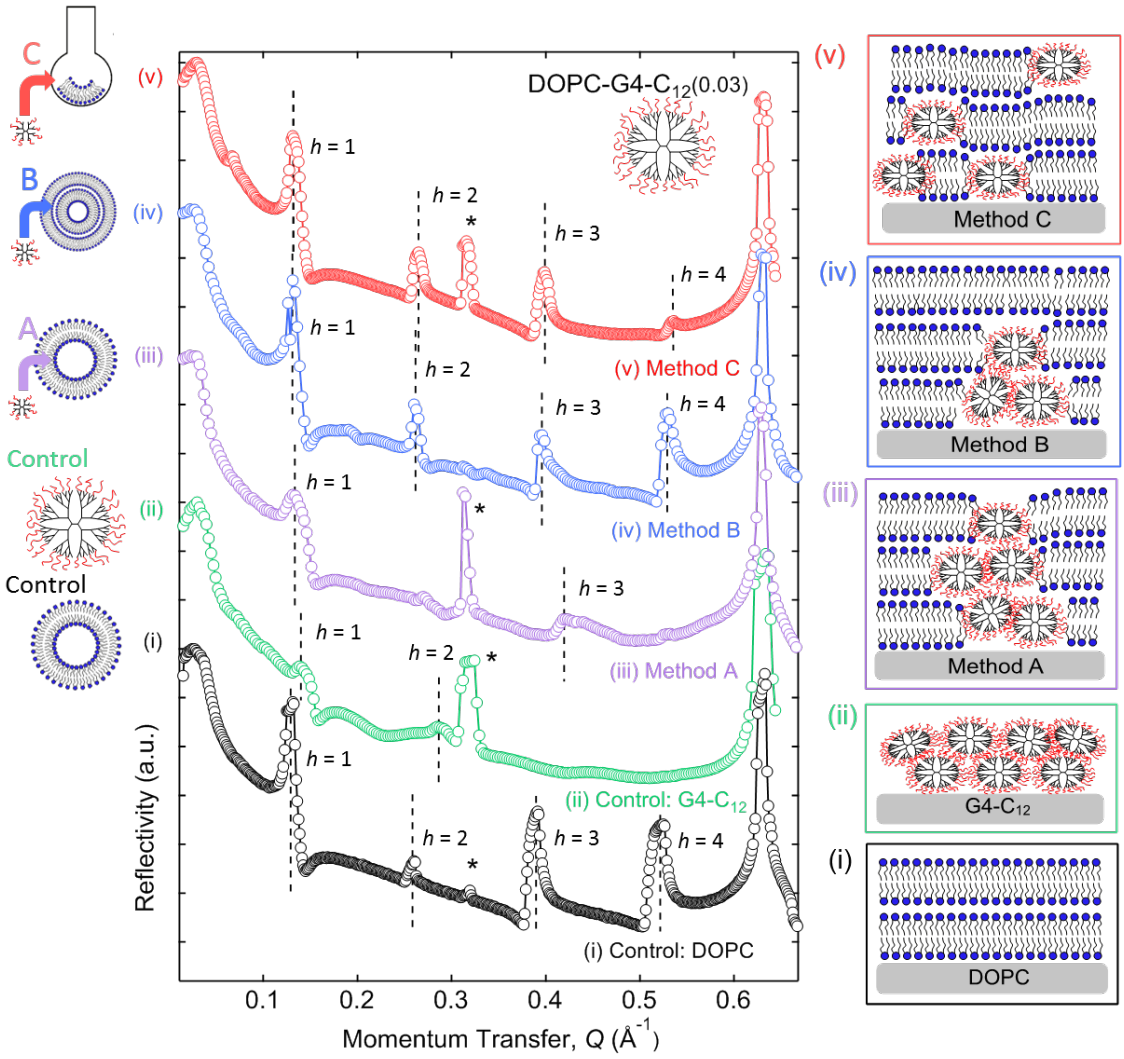

Figure 4. Reflectivity profiles for (i) SUV DOPC multilayers, (ii) G4 PAMAM dendrimers control , and (iii-v) DOPC-G4-C_{12}(0.03) multilayers made by incorporating dendrimers into DOPC lipid films (v, Method C) and MLV (iv, Method B) and SUV (iii, Method A) dispersions. Comparison of the positions of the Bragg peaks (*d*-spacing) and broadening of Bragg peaks (paracrystalline disorder *g* and coherence length L_s) is indicative of structural disorder caused by the incorporation of PAMAM dendrimers. Dotted lines indicate Bragg peak positions and are a guide for the eye. The forbidden half-Bragg of mica is marked with an asterisk (*) and the Bragg peaks associated with the multilayer structure are labelled with their reflection order (*h* = 1, 2, 3, and 4).

Compared to pure DOPC SUV multilayers (Fig. 4i), the dendrimer addition caused bilayer thinning, evident from smaller average *d*-spacing from all the mixing methods. Meanwhile, the spread of *d*-spacing increased: Method A, *d* = 41.0 - 51.6 Å; Method B, *d* = 46.3 - 49.7 Å; and Method C, *d* = 47.0 - 48.1 Å. The smallest average *d*-spacing was observed for Method A (*d* = 45.8 Å) a decrease of ~2.5 Å compared to DOPC-SUV multilayers (*d* = 48.3 Å), as can be seen clearly by the shifts in the *h* = 3 peaks in Figure 4iii. Small dendrimers have been shown to deform more against substrates (e.g. mica and lipid bilayers)[39, 60] due to their more open

and thus softer structure, whereas larger dendrimers would undergo smaller deformations because of steric hindrance of the denser branched amine groups on the surface. Both low generation dendrimers studied here (G2-C_{12} and G4-C_{12}) were likely deformed against mica and the lipid bilayers. It is worth noting that the bilayer thinning is an average decrease in *d*-spacing within the bilayer stack.

Multilayers from Method A (addition to SUVs) showed the largest structural disorder, evident from the greatest loss in the peak intensity and the greatest broadening of the Bragg peaks (*cf*. Figure 4iii). The coherence length for DOPC-G4-C_{12}(0.03)A (L_s = 190±70 Å) was significantly reduced compared to that for the control multilayers from DOPC SUVs (L_s = 2100±20 Å), indicating a less ordered structure. Due to their hydrophobic termination, these dendrimers could undergo aggregation as their aqueous dispersions (*cf*. Table 1 dendrimer size) were added to SUVs or MLVs in Methods A or B, respectively. Thus, the increased disorder in the multilayers from Method A could be attributed to the largest extent of dendrimer aggregation. Such an interpretation of dendrimer clustering is also consistent with the suggestion by Beddoes *et al.* [28] that nanoparticle clusters at the edges/boundaries of mesophase domains could be mediated by interactions between the nanoparticles and the membranes.

Method C (*cf*. Figure 4v) is expected to have resulted in a more homogeneous distribution of C_{12} dendrimers, due to dispersibility of the dendrimers in methanol. The larger coherence length (DOPC-G4-C_{12}(0.03)C; L_s = 1800±100 Å) compared to Method A (DOPC-G4-C_{12}(0.03)A; L_s = 190±70 Å) indicates more structural order. Method B (DOPC-G4-C_{12}(0.03)B; Figure 4iv) had a much higher L_s value (L_s = 2540±10 Å) compared to the other two mixing methods, which is comparable to that of the multilayers formed with DOPC SUVs (L_s = 2800±100 Å). This suggests that the multilayer structure was not significantly affected by the presence of dendrimers mixed using Method B, possibly due to homogenization by the extrusion process which suppressed dendrimer aggregation and improved dendrimer-lipid mixing.

The smaller G2-C_{12} dendrimers (size 2.8–3.3 nm) caused less disruption to the DOPC multilayer structure than the larger G4-C_{12} dendrimers (size 7.1 nm) above. For instance, all the Bragg peaks remained distinct for the DOPC-G2-C_{12}(0.127) multilayers (Figure 5i-iii) prepared using the three different mixing methods. The Scherrer coherence lengths (*cf*. Table S6–S7, SM) for DOPC-G2-C_{12}(0.127) multilayers are: Method A, L_s = 1100±100 Å; Method B, L_s; 900±100 Å; and Method C, L_s = 970±80 Å. These are smaller compared to the control DOPC-SUV multilayers (L_s = 2800±100 Å), but larger compared to the multilayers containing larger G4-C_{12} dendrimers.

Bilayer thinning was also observed for DOPC-G2-C_{12}(0.127) multilayers as compared to pure DOPC-SUV multilayers: Method A, *d* = 43.1-46.4 Å; Method B, *d* = 46.3-48.2 Å; Method C, *d* = 42.6-43.6 Å. Mixing Method C resulted in the largest *d*-spacing reduction of Δd = 3.7 Å between ν = 0.0063 and ν = 0.127, which could be attributed to more homogenous dendrimer-lipid mixing upon adding the hydrophobic dendrimers in a chloroform/methanol mixture (Method C).

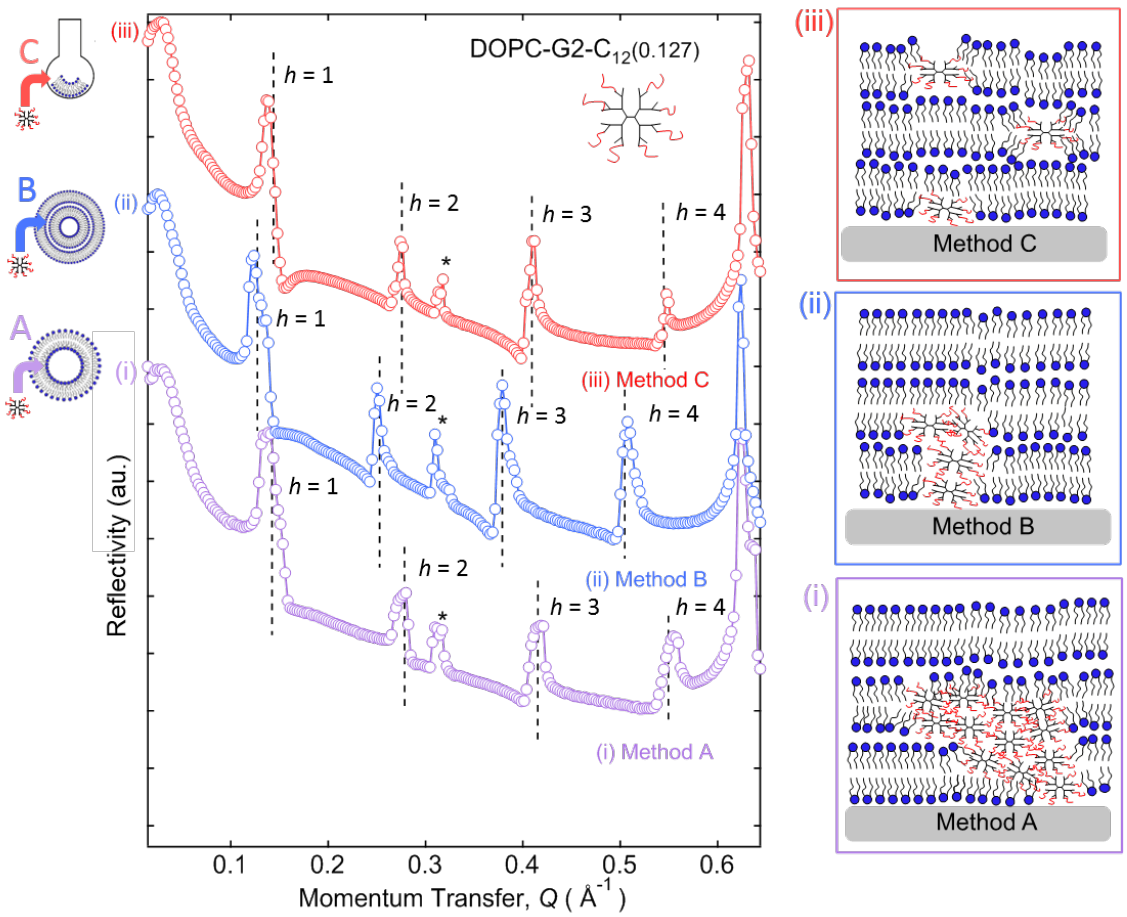

Figure 5. Reflectivity profiles of DOPC-G2-C_{12}(0.127) multilayers made by incorporating dendrimers into (i) SUVs (Purple, Method A), (ii) MLVs (Blue, Method B), and (iii) DOPC lipid films (Red, Method C) before drop-casting. The forbidden half-Bragg of mica is marked with an asterisk (*) and the Bragg peaks associated with the multilayer structure are labelled with their reflection order (h = 1, 2, 3, and 4).

Unlike DOPC-G4-C_{12}(0.03) multilayers, the lowest L_s and d-spacing values were observed for DOPC-G2-C_{12}(0.127)C multilayers (d = 43.3 Å, L_s = 970±80 Å). This points to the complexity of the size-dependent interactions between the dendrimers and the liposomes – the smaller dendrimers appeared more effective in infiltrating the bilayers by direct incorporation to the liposomes (Method C); whereas the larger dendrimers caused the most pronounced structural disruption with Method A, presumably due to their significant aggregation in aqueous media.

In addition to the Scherrer analysis, we have also attempted to fit the XRR curves using Parratt's recursion algorithm with a lipid multilayer model on mica [51, 52], with an example shown in Figure S9 in SM. However, the large surface roughness and non-uniformity in the multilayer films meant that the fit did not yield any reliable structural information additional to the findings using the Scherrer analysis.

3.2 Effect of dendrimer/lipid number ratio (ν) on the multilayer structure

Figure 6a shows that, for all the mixing methods and ν values, the coherence length L_s was lower than that of the control pure DOPC-SUV multilayers (dashed line in Figure 6a), indicating a loss in the DOPC multilayer structural order after the addition of G2-C_{12} dendrimers at all ν studied. The $L_s - \nu$ trend, however, was not clear-cut and depended on the dendrimer mixing method. An exception is in the case of Method C (Figure 6a) , where the coherence length L_s was found to decrease with increasing ν of G2-C_{12} dendrimers (see also Table S7, SM). For example, compared to DOPC-G2-C_{12}(0.00063)C multilayers, there was an L_s decrease, ΔL_s ~260 Å, for DOPC-G2-C_{12}(0.0063)C, and a further ΔL_s ~ 610 Å for DOPC-G2-C_{12}(0.127)C. This suggests that the smaller G2 dendrimers, with a size ~2.8-3.3 nm comparable to the thickness of the hydrophobic tail region of the DOPC bilayers, could be effectively incorporated into the multilayers. This is particularly true in the case of Method C in which the G2-C_{12} dendrimers were mixed with the lipids before hydration, and more dendrimers were intercalated in the membranes as ν increased (*cf*. Figure 8). The lack of a clear-cut trend in the case of Method A consistent with our suggestion above that dendrimer aggregation occurred in aqueous media (*cf*. Figure 8).

DOPC-G4-C_{12} multilayers at high ν had L_s values lower than that of the pure DOPC-SUV multilayers (*cf.* Figure 6b) where the lowest L_s value was observed for DOPC-G4-C_{12}(0.03) multilayers mixed using Method A (L_s ~ 200 Å). This highest structural disorder is consistent with the suggestion that G4-C_{12} aggregation is caused by mixing method A prior to multilayer formation. However, at low ν, L_s again depended on the mixing methods. At the lowest ν, addition of G4-C_{12} dendrimers to MLVs before extrusion (Method B) resulted in an increase in the coherence length to L_s ~ 5000 Å, whereas addition to lipid films (Method C) resulted in an L_s ~ 3000 Å for DOPC-G4-C_{12}(0.00015), comparable to that of DOPC-SUV (L_s ~ 2800 Å). Finally, addition to the SUVs (Method A) resulted in the greatest reduction in L_s for DOPC-G4-C_{12}(0.00015) multilayers to L_s ~ 1200 Å. It is interesting to note that Method B consistently produced the largest L_s of the three mixing methods for DOPC-G4-C_{12} multilayers which could be due to a decrease in dendrimer concentration due to dendrimer aggregates being too large to go through the polycarbonate membranes during extrusion. Different values of L_s were observed for other resolved Bragg peaks, as shown in Table S6–S7 in the SM, and followed similar trends.

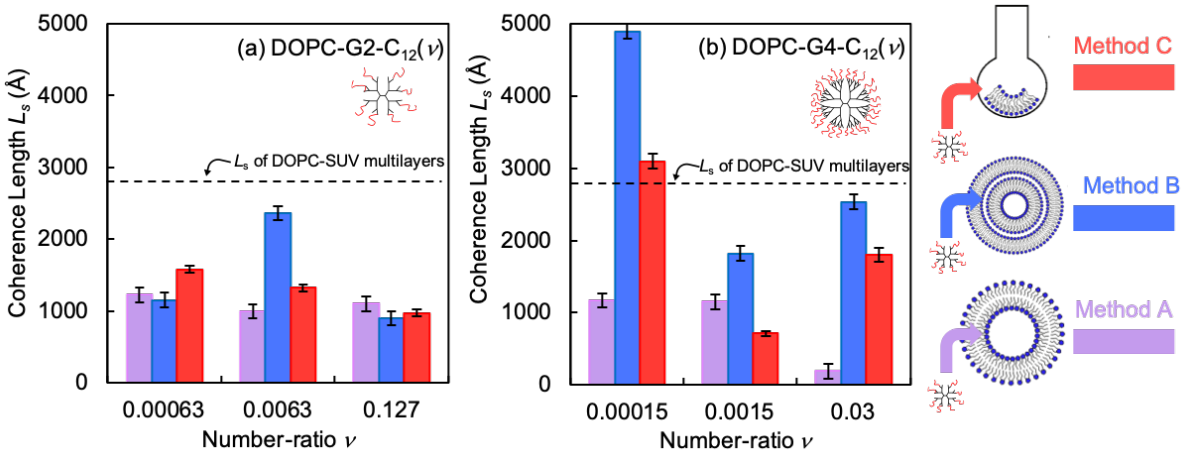

Figure 6. Dendrimer-to-lipid number ratio ν dependence of the Scherrer coherence length L_s for (a) DOPC-G2-C_{12}(ν) and (b) DOPC-G4-C_{12}(ν) multilayers. L_s was obtained from the first polymorph peak resolved from the h = 1 Bragg peak (1,0). The dashed line shows the L_s value for the pure DOPC multilayers. Dendrimers were added to DOPC lipid films (Red, Method C), MLVs (Blue, Method B) and SUVs (Purple, Method A) dispersions before drop-casting for comparison. Error δL varies with fitting of FWHM but in all cases is < 10%. Full tabulated data for all resolved peaks can be found in Table S6–S7 in the SM.

Figure 7a shows that, for DOPC-G2-C_{12} multilayers, with increasing ν the spread of d-spacing increased (Figure 7a: error bars) and the average d-spacing decreased. That is, the bilayer thinning effect was more pronounced upon increasing the amount of the smaller G2-C_{12} dendrimers. The d-spacing change (Δd = 0.1–0.7 Å) was very small for the lower dendrimer-lipid number ratios (ν = 0.00063 and ν = 0.0063) for all the mixing methods (A, B & C). However, for ν = 0.127, Δd = 1.6–3.7 Å was much larger. Considering corresponding changes in L_s discussed above, this represents a decrease in the number of stacked bilayers within the coherently scattering multilayer domain (calculated using the Scherrer analysis) from m ~ 33 for DOPC-G2-C_{12}(0.00063)C to m ~ 22 for DOPC-G2-C_{12}(0.127)C compared to m ~ 56 for DOPC-SUV multilayers (Table S3 and Table S8, SM). Since both d-spacing and coherence length are used to calculate m ($m = \frac{L_s}{d}$), the change in m with concentration mirrors that of the coherence length (*cf*. Figure 6a).

The ν dependence of bilayer thinning is less significant for the DOPC-G4-C_{12} multilayers (*cf*. Figure 7b), with a Δd ~ 0 - 1.6 Å between ν = 0.0015 to 0.03. However, for DOPC-G4-C_{12}(0.03)A (Table S5, SM), the decrease in the intensity and broadening of the Bragg peaks indicated increased disorder, evident from reduced L_s values (L_s = 190 Å) and a larger error on the *average* d-spacing (d = 45.8±0.9). This could be due to the dendrimers not mixing well with DOPC multilayers; instead, dendrimer aggregation on the mica surface prevented ordered templating of lipid multilayers (*cf*. Figure 8). This would result in a large reduction in L_s, but a smaller effect on the average d-spacing as observed here.

The bilayers in proximity to the dendrimer aggregates may have had different hydration levels to those further away, as a result of interactions with hydrophobic chains or exposed charged groups of the dendrimers, resulting in differences in *d*-spacing, also manifesting in an increased paracrystalline disorder. A film of G4-C_{12} dendrimers on mica was found to have some structural order, as discussed in Section S5 in the SM, with a *d*-spacing of d_1 = 44.4±0.1 Å (*m* ~ 8 layers). This value corresponds to the lowest bound of the *d*-spacing range observed for DOPC-G4-C_{12}(0.03) multilayers. G4-C_{12} have more hydrophobic C_{12} chains than G2-C_{12} dendrimers (G2; ~8, G4; ~32), and this increased hydrophobicity may result in greater aggregation of dendrimers in water that would lead to more ordered films upon drying as observed for G4-C_{12} films on mica. Increased hydrophobicity has been shown to increase intercalation of NPs into model membranes using MD simulations[33]. However, extensive dendrimer aggregation in water may reduce this effect as individual dendrimers would not be available for intercalation and intercalation of large aggregates would not be energetically favourable due to exposure of hydrophobic phospholipid alkyl chains to water (*cf*. Figure 8).

The *d*-spacing range (Figure 7b: error bars) increased with ν, which was also observed for DOPC-G2-C_{12} multilayers, for mixing methods A and B. Mixing method C was the exception, as these G4-C_{12} mixed multilayers had a narrower *d*-spacing range at high ν. There is also a decrease in the lower bound of the *d*-spacing range for methods A and B compared to DOPC-SUV (grey shaded area; Figure 7b), which corresponds to the decrease in average *d*-spacing.

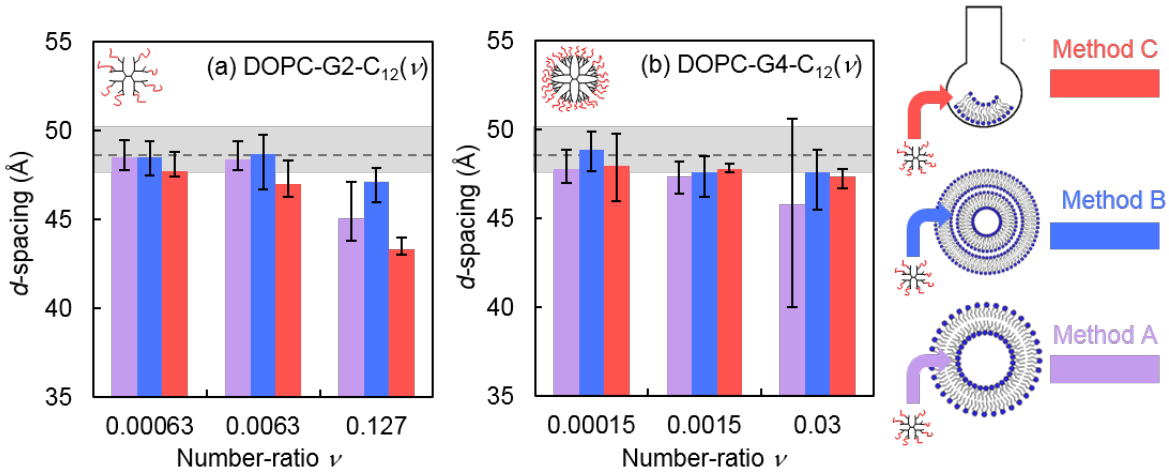

Figure 7. Dendrimer-to-lipid number ratio ν dependence of the average *d*-spacing for (a) DOPC-G2-C_{12}(ν) and (b) DOPC-G4-C_{12}(ν) multilayers. The error bars indicate the spread of *d*-spacing values for each mixing method. The dashed line represents the average *d*-spacing of DOPC-SUV multilayers, and shaded grey region represents the range. Dendrimers were added to DOPC lipid films (Red, Method C), MLVs (Blue, Method B) and SUVs (Purple, Method A) dispersions before drop-casting for comparison. Error in average δd = ± 0.1 Å. Full tabulated data for all resolved peaks can be found in table S5 in the SM.

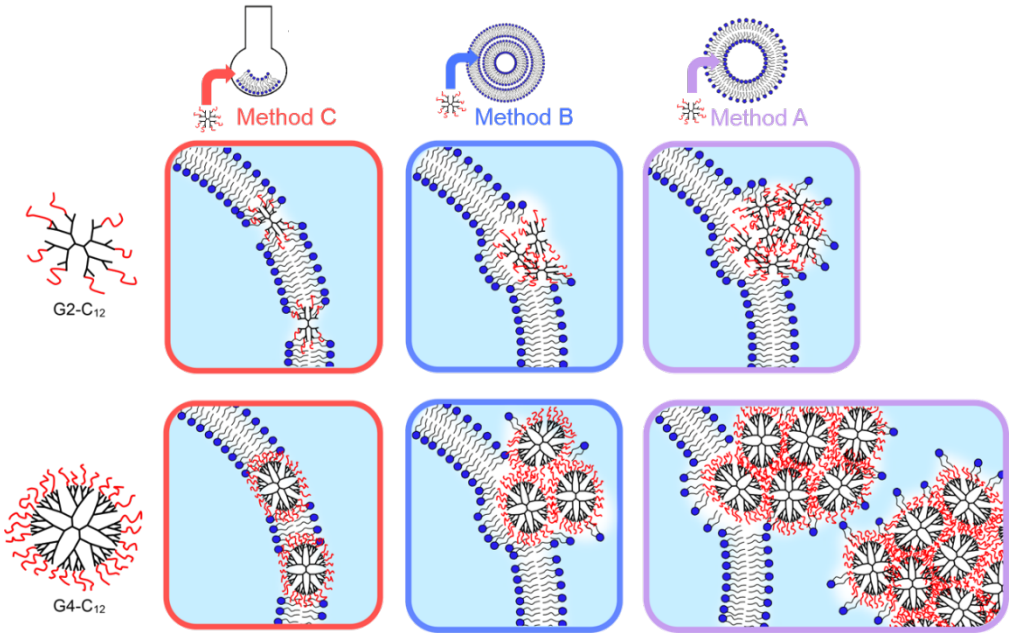

Figure 8. Cartoon to illustrate dendrimer intercalation into lipid bilayers in solution using mixing Method C, and dendrimer aggregation in Methods A and B where clusters interact with membranes.

3.3 Further discussion: NP 'snorkelling' and bilayer thinning

The more pronounced bilayer thinning (i.e. greater reduction in *d*-spacing) due to the presence of G2-C_{12} dendrimers (Δd = 1.6–3.7 Å) compared to G4-C_{12} dendrimers (Δd = 0–1.6 Å) could have been the result of the greater number of G2-C_{12} dendrimers in the multilayers (G2, ν = 0.127; G4, ν = 0.03). Previously, Au NPs coated in ligands of differing length [octanethiol (OT), heptadecanethiol (HDT), and 11-mercapto-1-undecanesulfonate (MUS)] were found to 'snorkel' into a lipid bilayer, resulting in thinner regions of the bilayer termed "pinch points" [61, 62]. This was postulated to occur due to the favourable interactions between the hydrophobic ligands and the hydrophobic lipid tail-groups, modulated by the unfavourable interactions between the charged Au core and the hydrophobic regions. This resulted in a cut-off size (< 4.5 nm) of Au NPs that would be inserted into the membrane. This could also be an explanation for the difference in bilayer thinning observed for G2-C_{12} and G4-C_{12} dendrimers.

Bilayer thinning results in increased structural disorder in the lipid tail-groups due to the formation of chain packing defects and an increase in the surface area per lipid. The burial of a charge into lipid bilayers would also raise an energy penalty, as translocation requires the formation of water defects as the ions remain solvated. Nonetheless, charged particles coated with flexible hydrophobic ligands have been shown to insert into bilayers in several MD simulations [61-63].

Interactions between the internal hydrophobic groups of the dendrimers and the hydrophobic lipid tails have been identified as the driving force of NH_2-dendrimer intercalation into fluid

phase bilayers [33]. These interactions can only occur if the dendrimer deforms from a spherical shape to make these hydrophobic moieties accessible. It follows that, for a dendrimer with a greater number of hydrophobic groups (such as C_{12} or acetamide (Ac) terminated dendrimers), internalisation would be more favourable in order to shield these groups from charges (*cf*. Figure 8). This was reported in an MD study by Kelly *et al.* [33] who observed a greater change in the radius of gyration (or flattening) of dendrimers with Ac functionalisation in contact with fluid phase bilayers compared to NH_2 terminated dendrimers. Fluid bilayers were found to form a concave depression that accommodated a greater area for dendrimer-bilayer interactions, resulting in twice as many interactions between dendrimers and bilayers in the fluid phase compared to the gel phase.

3.4 Effect of dendrimer surface chemistry on multilayer structure

The results described above were from mixtures containing dendrimers with 50% hydrophobic C_{12} terminations. The effect of dendrimer surface chemistry (or functionalisation) on DOPC multilayer structure was also studied by the addition of 100% amine terminated dendrimers (G2-NH_2 and G4-NH_2) to DOPC SUVs and drop cast to form multilayers. Amine terminated dendrimers have a smaller diameter (G2-NH_2, 2.1-2.3 nm; G4-NH_2, 3.8 nm) compared to those with additional C_{12} functionalisation (G2-C_{12}, 2.8-3.3 nm; G4-C_{12}, 7.1 nm) which could also influence their interactions due to the size effect. Furthermore, G2-NH_2 have 16 terminal amine groups and G4-NH_2 have 64, with 50% of these terminal groups conjugated with hydrophobic C_{12} chains for G2-C_{12} and G4-C_{12} dendrimers. The NH_2 dendrimers were added prior to the drying of the lipid film (i.e. only Method C was used; *cf*. Figure 1), and the results could be compared directly to DOPC-C_{12} multilayers mixed also using Method C.

Overall, addition of the NH_2-terminated dendrimers reduced structural order in the multilayers, evident from the loss of Bragg peak intensity for DOPC-NH_2 multilayers (*cf*. Figure S5, SM) compared to DOPC-SUV/MLV, and this is similar to that observed for DOPC-C_{12} multilayers (*cf*. Figure 4 and Figure 5).

Interestingly, the greatest change in *d*-spacing compared to the DOPC-SUV multilayers was observed for the DOPC-G2-NH_2(0.2)C multilayers (*cf*. Figure S5b, SM) with a shift from d = 50.07±0.1 Å to d = 40.00±0.1 Å for peak (1,0) and a decrease in the average *d*-spacing from d = 48.5±0.2 Å to d = 39.6±0.2 Å. This decrease (Δd ~10 Å) was the largest of all the multilayers studied, indicating a substantial thinning of lipid bilayers due to the presence of the smallest dendrimer NPs (theoretical diameter G2-NH_2 ~ 2.9 nm). This corroborates with the hypothesis discussed above that the G2-NH_2 dendrimer NPs could have caused 'pinch points' in the lipid bilayers upon their insertion. It is interesting to note here that for hydrated POPE lipid mesophases [30] the presence of G2-NH_2 and G4-NH_2 resulted in substantial bilayer swelling, in contrast to the thinning effect of these dendrimers on dried lipid multilayers.

Membrane thinning, and pore formation, was found to occur in DMPC SLBs in the presence of a variety of cationic polymer NPs by Leroueil *et al.* [64]. Other studies by this group determined that G3-NH_2 PAMAM dendrimers aggregated at existing defects of the bilayer, whereas G5-

NH_2 dendrimers expanded existing defects and G7-NH_2 formed new defects [36, 65]. Mecke *et al.* also observed thinning of DMPC SLBs on mica in the presence of a charged antimicrobial peptide MSI-78 (MW = 2476.63 Da) using AFM and NMR [66]. ^{2}H NMR of DMPC-d_{54} MLVs also revealed that the peptide interacted with the lipid headgroup region of DMPC and the hydrophobic chains were highly disordered.

Since only two ν values of G2-NH_2 and G4-NH_2 were studied, it was difficult to ascertain if there was a significant trend in *d*-spacing related to the ν of NH_2 dendrimers. However, plotting of the maximum and minimum values of *d*-spacing versus ν for DOPC-G2-NH_2 multilayers (*cf*. Figure S6b, SM) compared to the DOPC-SUV multilayers (*cf*. Figure S6b, SM; dashed line) showed no significant change in the range of *d*-spacing measured. This is indicative of no significant change in the paracrystalline disorder (*d*-spacing fluctuations). As described above, there was a decrease in the average *d*-spacing of multilayers at the highest ν (0.2) studied of G2-NH_2 dendrimers. For DOPC-G4-NH_2(0.2)C multilayers (*cf*. Figure S6a SM), the *d*-spacing was comparable (*d* = 48.3±0.1 Å), to that of the DOPC-SUV multilayers (*d* = 48.5±0.2Å) and polymorphism appeared reduced, as the spread of *d*-spacing values decreased at high ν. At low ν (0.02) the *d*-spacing was reduced (*d* = 43.6±0.2 Å), compared to DOPC-SUV multilayers. In order to ascertain a correlation with ν, a greater range of ν would need to be studied.

L_s of DOPC-Gi-NH_2C multilayers was also analysed (red circles; Figure S7 in SM). Overall, it was smaller than the control DOPC-SUV multilayers (dotted line; Figure S7) and decreased with increasing ν. Since only two ν values of NH_2 dendrimers were studied it is not possible to confirm if there was an overall trend. However, from the data points obtained, L_s was found to be smallest at the highest ν, as discussed in Section S15 in SM.

4. Summary and concluding remarks

DOPC-SUV and DOPC-MLV multilayers were prepared as control samples and studied using XRR, with *d*-spacings and the coherence length L_s values consistent with those from the literature[50]. Overall the addition of G2 and G4, -NH_2 or -C_{12} dendrimers to DOPC multilayers resulted in bilayer thinning and a decrease in structural order (decreased L_s) compared to pure DOPC multilayers. These effects were more pronounced when more dendrimers were added.

4.1 Effect of mixing method

Addition of G4-C_{12} to DOPC-SUVs after extrusion (Method A) resulted in the greatest disruption of DOPC multilayer order (decrease in L_s) postulated to be due to dendrimer aggregation and less homogenous mixing compared to addition before extrusion (Method B) and addition to lipid films followed by hydration and extrusion (Method C). However, for G2-C_{12} the greatest reduction in L_s was from samples made using mixing Method C, which could indicate more effective incorporation of smaller G2-C_{12} dendrimers into the multilayer using this method.

4.2 Effect of dendrimer size

G4-C_{12} dendrimers caused more disruption to the DOPC multilayer structural order than G2-C_{12} dendrimers (decrease in coherence length, L_s). However, G2-C_{12} caused more pronounced

bilayer thinning, an effect that could be compared with Au NPs coated with different ligands 'snorkelling' into a lipid bilayer, resulting in thinner regions of the bilayer or pinch points [61, 62].

4.3 Effect of dendrimer number ratio

Overall, increasing the number ratio of G2-C_{12} dendrimers resulted in more pronounced bilayer thinning (up to Δd = 3.7 Å, between ν = 0.0063 and ν = 0.127 for Method C) and increased structural disorder. This number ratio dependence of bilayer thinning was less significant for the DOPC-G4-C_{12} multilayers. However qualitatively, the dramatic loss of the Bragg peak intensity and peak broadening indicates increased disorder of the multilayer structure for the higher number ratios of G4-C_{12} mixed using Method A. The *d*-spacing range was also found to increase with ν, also observed for DOPC-G2-C_{12} multilayers, for mixing methods A and B, indicating increased paracrystalline disorder or polymorphism.

4.4 Effect of dendrimer surface functionalisation

The greatest bilayer thinning was observed for DOPC-G2-NH_2(0.2)C at Δd ~ 10 Å, indicating a substantial thinning of lipid bilayers due to the presence of the smallest dendrimer NPs (G2-NH_2; 2.9 nm). This corroborates with the idea that 'pinch points' are formed through dendrimer penetration into the bilayer, resulting in a reduction in the average bilayer *d*-spacing.

Overall, these results show the complexity of the effect of dendrimer physicochemical properties and the addition method of dendrimers on the structure of mixed dendrimer-DOPC multilayers. These parameters are important when considering multilayer hybrid materials for drug delivery, as well as to understanding the fundamental interactions that occur during dendrimer cell entry. We have reported the complex behaviour of lipid multilayers in the presence of dendrimers, particularly induced structural disorder and bilayer thinning. These insights are useful for the future biomedical application of dendrimers and other NPs, and for nanocomposite multilayer materials in which NPs are added to achieve enhanced properties or functionality.

5. Acknowledgements

Funding from the Engineering and Physical Science Research Council (EPSRC EP/L016648/1; L.J.F.), Procter & Gamble (A.S.), and Infinuem and the Everett Bequest Fund (N.T.) is gratefully acknowledged. The XRR was performed at the ESRF BM28 (XMaS) beamline, which is a mid-range facility supported by EPSRC. We are grateful to all the beamline team staff for their support.

6. References

[1] N.T. Pourianazar, P. Mutlu, U. Gunduz, Bioapplications of poly(amidoamine) (PAMAM) dendrimers in nanomedicine, J Nanopart Res 16(4) (2014).
[2] G.A. Pilkington, J.S. Pedersen, W.H. Briscoe, Dendrimer nanofluids in the concentrated regime: from polymer melts to soft spheres, Langmuir 31(11) (2015) 3333-42.

[3] R.W. Scott, O.M. Wilson, R.M. Crooks, Synthesis, characterization, and applications of dendrimer-encapsulated nanoparticles, The journal of physical chemistry. B 109(2) (2005) 692-704.
[4] N. Oddone, N. Lecot, M. Fernandez, A. Rodriguez-Haralambides, P. Cabral, H. Cerecetto, J.C. Benech, In vitro and in vivo uptake studies of PAMAM G4.5 dendrimers in breast cancer, J. Nanobiotechnol. 14 (2016) 12.
[5] G.S. Yu, Y.M. Bae, H. Choi, B. Kong, I.S. Choi, J.S. Choi, Synthesis of PAMAM dendrimer derivatives with enhanced buffering capacity and remarkable gene transfection efficiency, Bioconjug Chem 22(6) (2011) 1046-55.
[6] S.P. Mukherjee, M. Davoren, H.J. Byrne, In vitro mammalian cytotoxicological study of PAMAM dendrimers - towards quantitative structure activity relationships, Toxicol In Vitro 24(1) (2010) 169-77.
[7] S.P. Mukherjee, F.M. Lyng, A. Garcia, M. Davoren, H.J. Byrne, Mechanistic studies of in vitro cytotoxicity of poly(amidoamine) dendrimers in mammalian cells, Toxicol Appl Pharmacol 248(3) (2010) 259-68.
[8] G. Navarro, C. Tros de Ilarduya, Activated and non-activated PAMAM dendrimers for gene delivery in vitro and in vivo, Nanomed-Nanotechnol 5(3) (2009) 287-97.
[9] E. Markatou, V. Gionis, G.D. Chryssikos, S. Hatziantoniou, A. Georgopoulos, C. Demetzos, Molecular interactions between dimethoxycurcumin and Pamam dendrimer carriers, Int J Pharm 339(1-2) (2007) 231-6.
[10] K. Madaan, S. Kumar, N. Poonia, V. Lather, D. Pandita, Dendrimers in drug delivery and targeting: Drug-dendrimer interactions and toxicity issues, J Pharm Bioallied Sci 6(3) (2014) 139-150.
[11] L. Albertazzi, L. Gherardini, M. Brondi, S. Sulis Sato, A. Bifone, T. Pizzorusso, G.M. Ratto, G. Bardi, In vivo distribution and toxicity of PAMAM dendrimers in the central nervous system depend on their surface chemistry, Mol Pharmaceut 10(1) (2013) 249-60.
[12] M.K. Calabretta, A. Kumar, A.M. McDermott, C. Cai, Antibacterial activities of poly(amidoamine) dendrimers terminated with amino and poly(ethylene glycol) groups, Biomacromolecules 8(6) (2007) 1807-11.
[13] A.I. Lopez, R.Y. Reins, A.M. McDermott, B.W. Trautner, C. Cai, Antibacterial activity and cytotoxicity of PEGylated poly(amidoamine) dendrimers, Mol Biosyst 5(10) (2009) 1148-56.
[14] M. Ciolkowski, J.F. Petersen, M. Ficker, A. Janaszewska, J.B. Christensen, B. Klajnert, M. Bryszewska, Surface modification of PAMAM dendrimer improves its biocompatibility, Nanomedicine-Nanotechnology Biology and Medicine 8(6) (2012) 815-817.
[15] A. Janaszewska, M. Ciolkowski, D. Wrobel, J.F. Petersen, M. Ficker, J.B. Christensen, M. Bryszewska, B. Klajnert, Modified PAMAM dendrimer with 4-carbomethoxypyrrolidone surface groups reveals negligible toxicity against three rodent cell-lines, Nanomed-Nanotechnol 9(4) (2013) 461-4.
[16] M.A. Maher, H.J. Byrne, Modification of the in vitro uptake mechanism and antioxidant levels in HaCaT cells and resultant changes to toxicity and oxidative stress of G4 and G6 poly(amidoamine) dendrimer nanoparticles, Anal. Bioanal. Chem. 408(19) (2016) 5295-5307.
[17] R.M. Kannan, Perumal, O. P., and Kannan, S., Dendrimers and Hyperbranched Polymers for Drug Delivery, in: V.a.L.-P. Labhasetwar, D. L. (Ed.), Biomedical Applications of Nanotechnology, Wiley2007, p. 105.
[18] C. Montis, V. Generini, G. Boccalini, P. Bergese, D. Bani, D. Berti, Model lipid bilayers mimic non-specific interactions of gold nanoparticles with macrophage plasma membranes, J Colloid Interf Sci 516 (2018) 284-294.

[19] Z.Y. Zhang, B.D. Smith, High-generation polycationic dendrimers are unusually effective at disrupting anionic vesicles: Membrane bending model, Bioconjugate Chem 11(6) (2000) 805-814.
[20] K. Shimizu, A. Uchiyama, M. Yamashita, A. Hirose, T. Nishimura, N. Oku, Biomembrane damage caused by exposure to multi-walled carbon nanotubes, Journal of Toxicological Sciences 38(1) (2013) 7-12.
[21] X. Wei, W. Jiang, J. Yu, L. Ding, J. Hu, G. Jiang, Effects of SiO2 nanoparticles on phospholipid membrane integrity and fluidity, J Hazard Mater 287 (2015) 217-24.
[22] N. Abraham, E. Csapo, G. Bohus, I. Dekany, Interaction of biofunctionalized gold nanoparticles with model phospholipid membranes, Colloid Polym Sci 292(10) (2014) 2715-2725.
[23] A.P.a.B. Girard-Egrot, L. J., Langmuir-Blodgett Technique for Synthesis of Biomimetic Lipid Membranes, in: D.K. Martin (Ed.), Nanobiotechnology of Biomimetic Membranes, Springer, New York, 2007, pp. 23-74.
[24] S.J. Attwood, Y. Choi, Z. Leonenko, Preparation of DOPC and DPPC Supported Planar Lipid Bilayers for Atomic Force Microscopy and Atomic Force Spectroscopy, Int J Mol Sci 14(2) (2013) 3514-39.
[25] C.M. Bailey, E. Kamaloo, K.L. Waterman, K.F. Wang, R. Nagarajan, T.A. Camesano, Size dependence of gold nanoparticle interactions with a supported lipid bilayer: A QCM-D study, Biophys Chem 203-204 (2015) 51-61.
[26] P.R. Leroueil, S. Hong, A. Mecke, J.R. Baker, Jr., B.G. Orr, M.M. Banaszak Holl, Nanoparticle interaction with biological membranes: does nanotechnology present a Janus face?, Acc Chem Res 40(5) (2007) 335-42.
[27] M. Wlodek, M. Kolasinska-Sojka, M. Szuwarzynski, S. Kereiche, L. Kovacik, L.Z. Zhou, L. Islas, P. Warszynski, W.H. Briscoe, Supported lipid bilayers with encapsulated quantum dots (QDs) via liposome fusion: effect of QD size on bilayer formation and structure, Nanoscale 10(37) (2018) 17965-17974.
[28] C.M. Beddoes, J. Berge, J.E. Bartenstein, K. Lange, A.J. Smith, R.K. Heenan, W.H. Briscoe, Hydrophilic nanoparticles stabilising mesophase curvature at low concentration but disrupting mesophase order at higher concentrations, Soft Matter 12(28) (2016) 6049-57.
[29] J.M. Bulpett, T. Snow, B. Quignon, C.M. Beddoes, T.Y. Tang, S. Mann, O. Shebanova, C.L. Pizzey, N.J. Terrill, S.A. Davis, W.H. Briscoe, Hydrophobic nanoparticles promote lamellar to inverted hexagonal transition in phospholipid mesophases, Soft Matter 11(45) (2015) 8789-800.
[30] L.J. Fox, L. Matthews, H. Stockdale, S. Pichai, T. Snow, R.M. Richardson, W.H. Briscoe, Structural changes in lipid mesophases due to intercalation of dendritic polymer nanoparticles: Swollen lamellae, suppressed curvature, and augmented structural disorder, Acta Biomaterialia (2020) DOI: 10.1016/j.actbio.2019.12.036.
[31] J.M. Bulpett, A.M. Collins, N.H.M. Kaus, P.T. Cresswell, O. Bikondoa, D. Walsh, S. Mann, S.A. Davis, W.H. Briscoe, Interactions of nanoparticles with purple membrane films, J Mater Chem 22(31) (2012) 15635-15643.
[32] N.H.M. Kaus, A.M. Collins, O. Bikondoa, P.T. Cresswell, J.M. Bulpett, W.H. Briscoe, S. Mann, In situ X-ray reflectivity studies of molecular and molecular-cluster intercalation within purple membrane films, J Mater Chem C 2(27) (2014) 5447-5452.
[33] C.V. Kelly, P.R. Leroueil, B.G. Orr, M.M. Banaszak Holl, I. Andricioaei, Poly(amidoamine) dendrimers on lipid bilayers II: Effects of bilayer phase and dendrimer termination, The journal of physical chemistry. B 112(31) (2008) 9346-53.

[34] H. Lee, R.G. Larson, Molecular dynamics simulations of PAMAM dendrimer-induced pore formation in DPPC bilayers with a coarse-grained model, J. Phys. Chem. B 110(37) (2006) 18204-18211.
[35] X.C. He, Z.G. Qu, F. Xu, M. Lin, J.L. Wang, X.H. Shi, T.J. Lu, Molecular analysis of interactions between dendrimers and asymmetric membranes at different transport stages, Soft Matter 10(1) (2014) 139-148.
[36] A. Mecke, S. Uppuluri, T.M. Sassanella, D.K. Lee, A. Ramamoorthy, J.R. Baker, Jr., B.G. Orr, M.M. Banaszak Holl, Direct observation of lipid bilayer disruption by poly(amidoamine) dendrimers, Chem Phys Lipids 132(1) (2004) 3-14.
[37] A. Akesson, K.M. Bendtsen, M.A. Beherens, J.S. Pedersen, V. Alfredsson, M. Cardenas Gomez, The effect of PAMAM G6 dendrimers on the structure of lipid vesicles, Phys Chem Chem Phys 12(38) (2010) 12267-72.
[38] B. Klajnert, R.M. Epand, PAMAM dendrimers and model membranes: differential scanning calorimetry studies, Int J Pharm 305(1-2) (2005) 154-66.
[39] V. Tiriveedhi, K.M. Kitchens, K.J. Nevels, H. Ghandehari, P. Butko, Kinetic analysis of the interaction between poly(amidoamine) dendrimers and model lipid membranes, Biochim Biophys Acta 1808(1) (2011) 209-18.
[40] A. Akesson, T.K. Lind, R. Barker, A. Hughes, M. Cardenas, Unraveling dendrimer translocation across cell membrane mimics, Langmuir 28(36) (2012) 13025-33.
[41] X. He, Z. Qu, F. Xu, M. Lin, J. Wang, X. Shi, T. Lu, Molecular analysis of interactions between dendrimers and asymmetric membranes at different transport stages, Soft Matter 10(1) (2014) 139-48.
[42] L.J. Fox, R.M. Richardson, W.H. Briscoe, PAMAM dendrimer - cell membrane interactions, Adv Colloid Interface Sci 257 (2018) 1-18.
[43] C.M. Beddoes, C.P. Case, W.H. Briscoe, Understanding nanoparticle cellular entry: A physicochemical perspective, Adv Colloid Interface Sci 218 (2015) 48-68.
[44] N. Karoonuthaisiri, K. Titiyevskiy, J.L. Thomas, Destabilization of fatty acid-containing liposomes by. polyamidoamine dendrimers, Colloids and Surfaces B-Biointerfaces 27(4) (2003) 365-375.
[45] M. Kang, M. Tuteja, A. Centrone, D. Topgaard, C. Leal, Nanostructured Lipid-Based Films for Substrate-Mediated Applications in Biotechnology, Advanced Functional Materials (2018) 1704356.
[46] C.H. Lee, H. Kim, D.V. Harburg, G. Park, Y. Ma, T. Pan, J.S. Kim, N.Y. Lee, B.H. Kim, K.-I. Jang, S.-K. Kang, Y. Huang, J. Kim, K.-M. Lee, C. Leal, J.A. Rogers, Biological lipid membranes for on-demand, wireless drug delivery from thin, bioresorbable electronic implants, 7(11) (2015) e227.
[47] S.L. Perry, S.G. Neumann, T. Neumann, K. Cheng, J. Ni, J.R. Weinstein, D.V. Schaffer, M. Tirrell, Challenges in nucleic acid-lipid films for transfection, AIChE Journal 59(9) (2013) 3203-3213.
[48] G.R. Heath, M. Li, H. Rong, V. Radu, S. Frielingsdorf, O. Lenz, J.N. Butt, L.J.C. Jeuken, Multilayered Lipid Membrane Stacks for Biocatalysis Using Membrane Enzymes, Advanced Functional Materials 27(17) (2017) 1606265.
[49] L.A. Lautscham, C.Y. Lin, V. Auernheimer, C.A. Naumann, W.H. Goldmann, B. Fabry, Biomembrane-mimicking lipid bilayer system as a mechanically tunable cell substrate, 35(10) (2014) 3198-3207.

[50] B. Sironi, T. Snow, C. Redeker, A. Slastanova, O. Bikondoa, T. Arnold, J. Klein, W.H. Briscoe, Structure of lipid multilayers via drop casting of aqueous liposome dispersions, Soft Matter 12(17) (2016) 3877-87.
[51] W.H. Briscoe, F. Speranza, P.X. Li, O. Konovalov, L. Bouchenoire, J. van Stam, J. Klein, R.M.J. Jacobs, R.K. Thomas, Synchrotron XRR study of soft nanofilms at the mica-water interface, Soft Matter 8(18) (2012) 5055-5068.
[52] F. Speranza, G.A. Pilkington, T.G. Dane, P.T. Cresswell, P.X. Li, R.M.J. Jacobs, T. Arnold, L. Bouchenoire, R.K. Thomas, W.H. Briscoe, Quiescent bilayers at the mica-water interface, Soft Matter 9(29) (2013) 7028-7041.
[53] W.H. Briscoe, M. Chen, I.E. Dunlop, J. Klein, J. Penfold, R.M.J. Jacobs, Applying grazing incidence X-ray reflectometry (XRR) to characterising nanofilms on mica, Journal of colloid and interface science 306(2) (2007) 459-463.
[54] G.A. Pilkington, W.H. Briscoe, Nanofluids mediating surface forces, Adv Colloid Interfac 179 (2012) 68-84.
[55] W.H. Briscoe, Depletion forces between particles immersed in nanofluids, Curr Opin Colloid In 20(1) (2015) 46-53.
[56] A. Jesorka, O. Orwar, Liposomes: Technologies and Analytical Applications, 1(1) (2008) 801-832.
[57] M. Danaei, M. Dehghankhold, S. Ataei, F. Hasanzadeh Davarani, R. Javanmard, A. Dokhani, S. Khorasani, M.R. Mozafari, Impact of Particle Size and Polydispersity Index on the Clinical Applications of Lipidic Nanocarrier Systems, Pharmaceutics 10(2) (2018) 57.
[58] A.L. Patterson, The Scherrer formula for x-ray particle size determination, Phys Rev 56(10) (1939) 978-982.
[59] F.W. Jones, The Measurement of Particle Size by the X-Ray Method, 166(924) (1938) 16-43.
[60] T.A. Betley, M.M.B. Holl, B.G. Orr, D.R. Swanson, D.A. Tomalia, J.R. Baker, Tapping mode atomic force microscopy investigation of poly(amidoamine) dendrimers: Effects of substrate and pH on dendrimer deformation, Langmuir 17(9) (2001) 2768-2773.
[61] R.C. Van Lehn, P.U. Atukorale, R.P. Carney, Y.-S. Yang, F. Stellacci, D.J. Irvine, A. Alexander-Katz, Effect of Particle Diameter and Surface Composition on the Spontaneous Fusion of Monolayer-Protected Gold Nanoparticles with Lipid Bilayers, 13(9) (2013) 4060-4067.
[62] R.C. Van Lehn, A. Alexander-Katz, Membrane-Embedded Nanoparticles Induce Lipid Rearrangements Similar to Those Exhibited by Biological Membrane Proteins, J. Phys. Chem. B 118(44) (2014) 12586-12598.
[63] P. Gkeka, P. Angelikopoulos, L. Sarkisov, Z. Cournia, Membrane Partitioning of Anionic, Ligand-Coated Nanoparticles Is Accompanied by Ligand Snorkeling, Local Disordering, and Cholesterol Depletion, Plos Comput Biol 10(12) (2014).
[64] P.R. Leroueil, S.A. Berry, K. Duthie, G. Han, V.M. Rotello, D.Q. McNerny, J.R. Baker, B.G. Orr, M.M. Banaszak Holl, Wide Varieties of Cationic Nanoparticles Induce Defects in Supported Lipid Bilayers, Nano Letters 8(2) (2008) 420-424.
[65] A. Mecke, D.K. Lee, A. Ramamoorthy, B.G. Orr, M.M. Holl, Synthetic and natural polycationic polymer nanoparticles interact selectively with fluid-phase domains of DMPC lipid bilayers, Langmuir 21(19) (2005) 8588-90.
[66] A. Mecke, D.-K. Lee, A. Ramamoorthy, B.G. Orr, M.M. Banaszak Holl, Membrane Thinning Due to Antimicrobial Peptide Binding: An Atomic Force Microscopy Study of MSI-78 in Lipid Bilayers, Biophysical Journal 89(6) (2005) 4043-4050.

Supporting Materials (SM)

Interactions between PAMAM dendrimers and DOPC lipid multilayers: Membrane thinning and structural disorder

Laura J. Fox [a,b], Anna Slastanova [b], Nicolas Taylor [b], Magdalena Wlodek [c], Oier Bikondoa [d,e], Robert M. Richardson [f] and Wuge H. Briscoe [b*]

a Bristol Centre for Functional Nanomaterials, H. H. Wills Physics Laboratory, University of Bristol, Tyndall Avenue, Bristol BS8 1TL, UK

b School of Chemistry, University of Bristol, Cannock's Close, Bristol BS8 1TS, UK

c Jerzy Haber Institute of Catalysis and Surface Chemistry, Polish Academy of Sciences, Niezapominajek 8, PL-30239 Krakow, Poland

d XMaS, The UK-CRG Beamline, The European Synchrotron (ESRF), 71 Avenue des Martyrs, 38043 Grenoble, France

e Department of Physics, University of Warwick, Gibbet Hill Road, Coventry CV4 7AL, UK

f School of Physics, H. H. Wills Physics Laboratory, University of Bristol, Tyndall Avenue, Bristol BS8 1TL, UK

*Email: wuge.briscoe@bristol.ac.uk, Tel: +44 (0)117 3318256

S1. Data analysis methods

This analysis was performed using peaking fitting software within IGOR Pro (*cf.* Figure 3a, DOPC-G2-C_{12}(0.127) Method A). The final Bragg peak observed at ~ Q = 0.63 Å was the Bragg peak of the mica substrate, and mica's forbidden half-Bragg was present in some of the curves marked with an asterisk (*) and is due to the mica unit cell encompassing two lattice layers. Bragg peaks labelled h = 1 to 4 were present for DOPC-G2-C_{12}(0.127) multilayers (mixed using method A) due to the multilayer structure on the surface of the mica (*cf.* Figure 3a). The equal spacing of these peaks is indicative of a lamellar phase, as expected by the DOPC lipids at RT [1]. The Bragg peaks consisted of three Gaussian peaks, indicating sample polymorphism (h = 1; Figure 3b), the peak positions Q_{hn} were used to calculate the lamellar d-spacing (*cf.* Figure 3d). The FWHM of the Gaussian peaks ΔQ_{hn} were used to calculate the coherence length (*cf*. Figure 3d) alongside peak broadening parameters which were plotted against h^4 for complementary peaks i.e. constant n (*cf*. Figure 3c). From the slope and gradient of a linear fit to this peak broadening plot, the coherence length and paracrystalline disorder parameter were calculated.

S2. DLS data table

Table S1. The mean hydrodynamic diameter (number distribution) and polydispersity index (PDI) of dendrimer-liposome mixtures measured using dynamic light scattering for two generations of dendrimers varying dendrimer functionality, concentration and mixing method.

Sample	Mixing Method	Mean Diameter (nm)	PDI
DOPC-MLV	MLV	93	1.0
DOPC-SUV	SUV	75	0.2
DOPC- G4-C_{12}(0.00015)	A	90	0.1
DOPC-G4-C_{12}(0.0015)		109	0.1
DOPC-G4-C_{12}(0.03)		55	0.2
DOPC-G2-C_{12}(0.00063)		55	0.2
DOPC-G2-C_{12}(0.0063)		115	0.3
DOPC-G2-C_{12}(0.127)		119	0.3
DOPC-G4-C_{12}(0.00015)	B	83	0.1
DOPC-G4-C_{12}(0.0015)		104	0.1
DOPC-G2-C_{12}(0.00063)		72	0.1
DOPC-G2-C_{12}(0.0063)		50	0.3
DOPC-G2-C_{12}(0.127)		255	0.4
DOPC-G4-C_{12}(0.00015)	C	90	0.1
DOPC-G4-C_{12}(0.0015)		100	0.1
DOPC-G4-C_{12}(0.03)		229	0.3
DOPC-G2-C_{12}(0.00063)		92	0.1
DOPC-G2-C_{12}(0.127)		159	0.3
DOPC-G4-NH_2(0.002)		231	0.4
DOPC-G4-NH_2(0.02)		55/358	0.6
DOPC-G2-NH_2(0.002)		4200	0.1
DOPC-G2-NH_2(0.02)		137	0.3

S3. DLS discussion

DLS was used to study the size distribution and polydispersity of liposome-dendrimer dispersions before drop-casting.

The addition method of combining the dendrimers with lipids affected the size and PDI of the liposomes. Mixing C_{12} terminated dendrimers with DOPC-SUV liposomes (Method A) resulted in the formation of smaller structures ~ 55 nm in size, which could be either dendrimer-lipid aggregates formed by dendrimers stripping lipids from liposomal bilayers or dendrimer aggregates in solution. G2-NH_2 terminated dendrimers at the lowest number ratio mixed with DOPC lipids (Method C) were found to cause larger aggregates (Table S1), which could be clusters of vesicles which agrees with results from Åkesson *et al.* [2] who observed POPC:POPG liposomes aggregated in the presence of G6-NH_2 dendrimers due to dendrimer bridging between the liposomes.

Tiriveedhi *et al.* [3] and Zhang and Smith[4] also observed the aggregation of vesicles due to bridging by NH_2-terminated dendrimers which was dendrimer concentration dependent. A larger concentration of dendrimers was postulated to result in the stabilisation of liposomes as the surface of the liposomes was saturated with dendrimers causing repulsion between liposomes, due to the dendrimers net positive charge. A low concentration of dendrimers could result in dendrimers bridging liposomes as they interacted with adjacent membranes, causing liposome aggregation.

Dendrimers mixed with DOPC using Method C mostly showed an increase in average diameter with the dendrimer concentration (exception DOPC-G2-NH_2), which supports the hypothesis that the dendrimers could have been attached to the outer leaflet of the liposomal bilayer. Method C was postulated to produce the most homogenous mixing of dendrimers with DOPC lipids, due to solubility of dendrimers and lipids in the chloroform:methanol mixture. This homogenous distribution may cause the increased aggregation of liposomes compared to the other mixing methods. Despite large aggregates present within some dendrimer-DOPC mixtures, all dispersions led to the formation of lipid multilayers (with varying structural properties) upon drop-casting the dispersions onto mica substrates. Therefore, there must be intact bilayers present within the dendrimer-lipid dispersions upon vesicle rupturing during the deposition and drying of the dispersions on to mica. The structure of the resultant multilayer formed by drop-casting of these dispersions was determined using XRR and will be discussed below.

S4. Structures of DOPC multilayers (without dendrimers) from SUVs and MLVs

S4.1 d-spacing and the Scherrer coherence length L_s

Pure DOPC multilayers at RT, prepared using SUVs, were studied using XRR as a control (Figure S1i). Four equally spaced Bragg peaks were observed before the mica Bragg peak at 0.63 $Å^{-1}$, corresponding to the reflection orders h = 1, 2, 3 and 4 of a lamellar phase. DOPC is known to have a gel to fluid transition temperature of -17 °C, and therefore was in the fluid lamellar phase at RT. The lamellar d-spacing was calculated using equation (2), and the discrete values are listed in Table S3. Each Bragg peak reflection could be resolved to 2 peaks (n), corresponding to two different d-spacings which indicated polymorphism. The d-spacing of the DOPC SUV multilayers (Figure S1i) ranged from 47.6 to 50.1 Å, with an average d-spacing d = 48.5±0.2Å, in agreement with the literature for a pure DOPC bilayer at ~45% relative humidity [5] and DOPC multilayers in similar conditions [1]. The range in d-spacing indicates sample polymorphism which could be a result of defects formed during drying. The coherence length derived from the Scherrer analysis of peak (h,n) = (1,0) was L_s = 2800±100 Å, which corresponds to m ~ 58 stacked bilayers (Table S3).

The d-spacing of the multilayers prepared using MLVs (Figure S1ii) was d = 47.3 to 50.1 Å with an average value d = 48.3±0.2 Å, very similar to those obtained for DOPC-SUV multilayers described above. The Scherrer coherence length from peak (1,0) was L_s = 2100±20 Å, which corresponds to m ~ 43 stacked bilayers (Table S4).

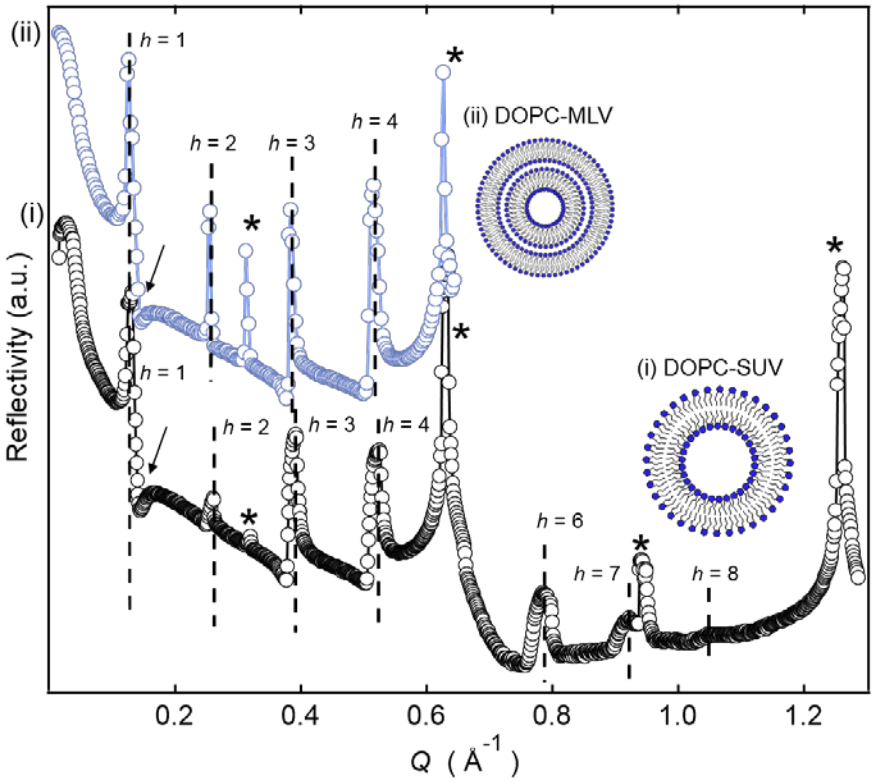

Figure S1. DOPC multilayers created by drop-casting (i) small unilamellar vesicles (SUVs) and (ii) and multi-lamellar vesicles (MLVs) on mica. The mica Bragg and half-Bragg are indicated by an asterisk (*). Negative peaks indicated by arrows are due to surface relaxation of the top bilayer at the air-film interface.

The smaller L_s values for multilayers created by drying MLVs compared to SUVs point to increased disorder in the multilayer structure. However, the difference in polymorphism between the samples was not as pronounced as multilayers analysed by Sironi *et al.* [1] who observed a larger spread in the *d*-spacing for the multilayers formed using MLVs (*d* = 46.6–50.9 Å) compared to those from the SUVs (*d* = 49.1–49.3 Å). The L_s values calculated here for SUV and MLV multilayers are of the same order of magnitude as those found by Sironi *et al.* (L_s ~2000 Å and L_s ~1400 Å, respectively) and the MLV multilayers show a similar decrease in L_s compared to the SUV multilayers. SUVs are expected to form a more uniform structural template on mica upon rupture, leading to a more organised structure in the dried multilayers compared to MLVs which are more polydisperse and frustrate packing upon rupture.

S4.2 Paracrystalline disorder in the pure DOPC multilayers

Two series of equally spaced Bragg peaks (*d* = 48.5 Å and 47.5 Å, respectively) were present in the XRR curves for DOPC-SUV multilayers due to polymorphism, with the corresponding two peak broadening plots shown in Figure S2. These two distinct sets (*h*,0) and (*h*,1) make the DOPC-SUV peaks appear broader than the DOPC-MLV peaks (Figure S1). Since up to *h* = 7 peak was recorded for the DOPC-SUV multilayers, it was possible to produce plots for both sets, although it was not possible to resolve both structural peaks at *h* = 6 and *h* = 2.

The *d*-spacing difference (~ 1 Å) between the two lamellar phases could be related to their different average hydration levels or slightly different chain packing, which would manifest in different long-range order of the multilayers. Bilayers at the surface may also have a reduced *d*-spacing due to surface relaxation which contributes to paracrystalline disorder. For the (*h,0*) peaks (d = 48.5 Å), the paracrystalline disorder parameter, coherence length, and the number of bilayers were calculated to be g = 0.026±0.007, L_b = 700±200 Å and m = 15±5, respectively (*cf*. Table S2, Figure S2). For the (*h,1*) peaks (d = 47.5 Å), the lamellar domains appear more ordered and the corresponding structural parameters were g = 0.0074±0.0008, L_b =1500±100 Å and m = 32±2, respectively.

There is a significant difference between the coherence length parameters calculated using Scherrer (L_s) and the peak broadening analysis (L_b). Despite differences in values L_b and L_s have been shown to follow the same trends previously [1]. Surprisingly, the DOPC-SUV multilayers had a smaller coherence length (L_b), calculated from peak broadening (700±200 Å and 1500±100 Å), than DOPC-MLV multilayers (2100±900 Å). This is inconsistent with the increased ordering expected for drop-cast DOPC-SUV multilayers also described in the literature [1]. However, due to large uncertainties in the calculation of the broadening coherence length L_b, its usage is limited in the discussion.

S5. Peak broadening plots of DOPC-SUV multilayers

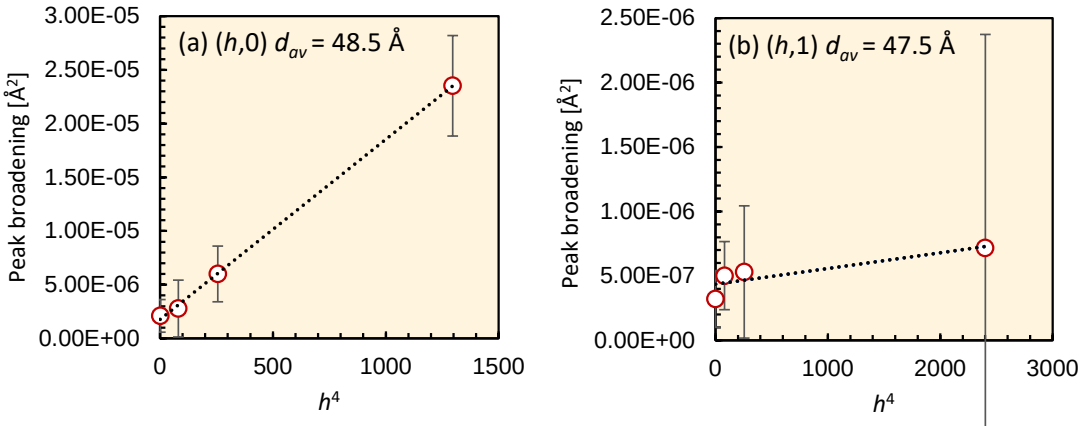

Figure S2. Peak broadening plots for DOPC-SUV multilayers. Two sets of equally spaced Bragg peaks indicated polymorphism and two peak broadening plots could be created from (a) set (h,0) and (b) set (h,1). The average *d*-spacing for these two sets had a difference of 1 Å. The gradient and intercept of a linear fit to these plots was used to calculate paracrystalline disorder g and broadening coherence length L_b respectively.

S6. G4-C_{12} film structure: Dendrimer control sample

A dispersion of pure G4-C_{12} dendrimers was dried onto mica as an additional control. For this sample, two small Bragg peaks were observed which indicated the presence of an ordered arrangement of dendrimers in the direction perpendicular to the mica surface. The *d*-spacings calculated from the position of these Bragg peaks were d_1 = 44.4±0.1 Å and d_2 = 21.8±0.1 Å (if h=2, d_2 = 43.6±0.1 Å). This is similar in size to the diameter obtained from the manufacturer (45 Å) of the G4-NH_2 dendrimer without hydrophobic functionalisation. It has been observed using AFM that dendrimers deform against mica[6], and therefore the reduced diameter on a substrate compared to the hydrodynamic diameter measured with DLS is not surprising (7.1 nm). The Scherrer analysis of the h = 1 and possible h = 2 Bragg peaks gives the coherence length L_s = 370±30 Å and 340±60 Å, respectively, and the corresponding number of layers m = 8±1.

S7. Paracrystalline disorder, *g*, and coherence length L_b

Table S2. Bilayer thickness, *d* and peak broadening analysis for XRR profiles of DOPC mixed dendrimer multilayers using three different dendrimer mixing methods (A, B and C), two generations of dendrimers (G2 and G4), two dendrimer terminal groups (NH_2 and C_{12}) and different dendrimer-lipid number ratios, ν. * Large errors due to the small number of points in peak broadening plots resulting in large fitting errors on linear regression.

Dendrimer-Lipid Number Ratio, ν	Bilayer Thickness, *d* (Å)	Paracrystalline Disorder, *g*	Coherence Length, L_b (Å)
Control Samples			
DOPC-SUV	47.6-50.1	0.026±0.007/0.0074±0.0008	700±200/1500±100
DOPC-MLV	47.3-50.1	0.02±0.02*	2100±900
G4-C_{12}	43.6-44.4	-	-
Method A: DOPC-G4-C_{12}			
0.00015	46.7-48.6	0.022±0.009	950±90
0.0015	46.6-48.4	0.032±0.011	1600±1800*
0.03	41.0-51.6	-	-
Method B: DOPC-G4-C_{12}			
0.00015	47.9-50.1	0.015±0.015*	2200±600
0.0015	46.7-49.0	0.016±0.01	1500±100
0.03	46.3-49.7	0.022±0.027	900±200
Method C: DOPC-G4-C_{12}			
0.00015	46.2-50.0	0.024±0.004	2250±10
0.0015	47.5-48.0	0.024±0.009	900±100
0.03	47.0-48.1	0.026±0.003	608±10
Method A: DOPC-G2-C_{12}			
0.00063	47.5-49.2	0.018±0.007	1400±100
0.0063	47.7-49.0	0.025±0.009	820±90
0.127	43.1-46.4	0.014±0.016*	1100±80
Method B: DOPC-G2-C_{12}			
0.00063	47.6-49.5	0.013±0.058*	1000±100
0.0063	47.6-50.7	0.016±0.016*	1300±200
0.127	46.3-48.2	0.024±0.002	1400±80
Method C: DOPC-G2-C_{12}			
0.00063	46.6-48.0	0.024±0.012	1500±600
0.0063	45.7-47.7	0.018±0.013*	1100±100
0.127	42.6-43.6	0.027±0.005	1300±100
Method C: DOPC-G4-NH_2			
0.02	42.8-44.1	-	-
0.2	48.0-48.4	0.015±0.02*	670±30
Method C: DOPC-G2-NH_2			
0.02	47.8-49.4	-	-
0.2	38.9-40.0	-	-

S8. DOPC SUV and MLV Scherrer analysis data tables

Table S3. Bragg peak positions, Q_{hn}, calculated *d*-spacing, full width at half maximum (FWHM), coherence length, L_s and number of layers, *m* for DOPC multilayers formed from SUVs. * Errors are large due to small number of points in peaks, resulting in larger errors in peak fitting and FWHM values.

h	n	Q_{hn} (Å^{-1})	*d* (Å) (± 0.1 Å)	FWHM	L_s (Å)	*m*
1	0	0.125	50.07	0.0023±0.0001	2800±100	56±2
	1	0.130	48.50	0.0051±0.0002	1250±60	26±1
	2	0.132	47.61	0.0016±0.0002	4000±600	80±10
2	0	0.256	49.15	0.006±0.003	1000±500	20±10
	1	0.258	48.65	0.0029±0.0008	2200±600	45±12
	2	0.261	48.20	0.0013±0.0004	5000±1000	100±20
3	0	0.388	48.56	0.00816±0.0003	770±30	16±1
	1	0.391	48.23	0.0038±0.0006	1600±300	33±6
	2	0.392	48.06	0.0017±0.0004	3700±700	80±20
4	0	0.516	48.67	0.0073±0.0007	860±80	18±2
	1	0.522	48.11	0.0074±0.0003	850±40	18±1
	2	0.526	47.80	0.0023±0.0002	2700±200	56±4
6	0	0.785	48.03	0.0208±0.0004	300±10	6±1
	1	0.796	47.33	0.0038±0.0005	1700±200	36±4
	2	-	-	-	-	-
7	0	0.920	47.82	0.02±0.02*	300±300	6±6

Table S4. Bragg peak positions, Q_{hn}, calculated *d*-spacing, full width at half maximum (FWHM), coherence length, L_s and number of layers, *m* for DOPC multilayers formed from MLVs.

h	n	Q_{hn} (Å^{-1})	*d* (Å) (± 0.1 Å)	FWHM	L_a (Å)	*m*
1	0	0.125	50.11	0.00299±0.00002	2100±20	42±1
	1	0.130	48.36	0.00408±0.00006	1540±20	32±1
2	0	0.254	49.46	0.00244±0.00002	2580±20	52±1
3	0	0.383	49.25	0.00180±0.00001	3450±10	70±<1
	1	0.385	48.97	0.0019±0.00001	3280±10	67±<1
4	0	0.513	48.99	0.0049±0.0001	1300±100	27±2
	1	0.516	48.75	0.0035±0.0001	1800±500	40±10

S9. Reflectivity curves DOPC-G2-C_{12}(ν) multilayers

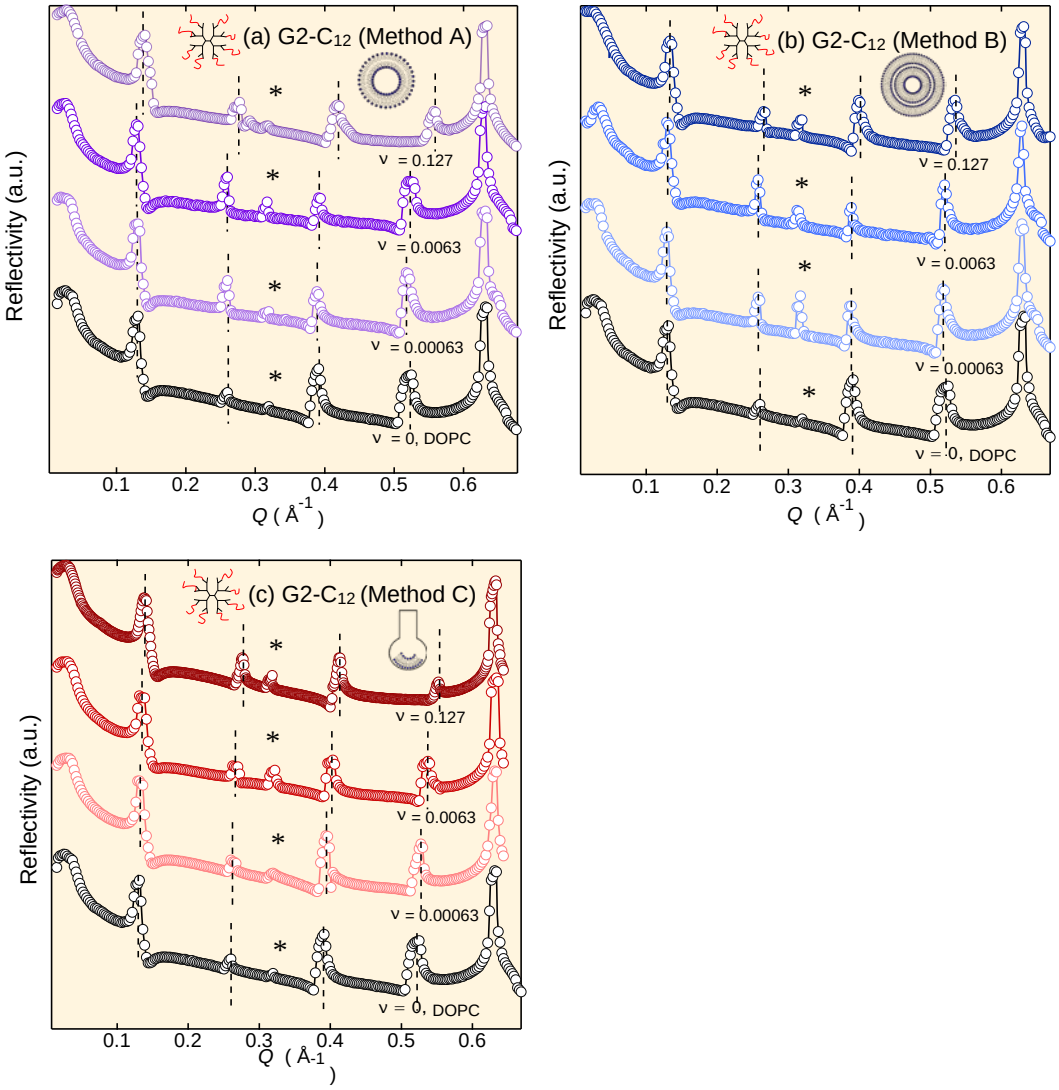

Figure S3. Reflectivity profiles of DOPC-G2-C_{12}(ν) multilayers at three number ratios (0.127, 0.0083 and 0.00083) made using mixing methods method A(a), B(b) and C(c).

S10. Reflectivity curves DOPC-G4-C12(ν) multilayers

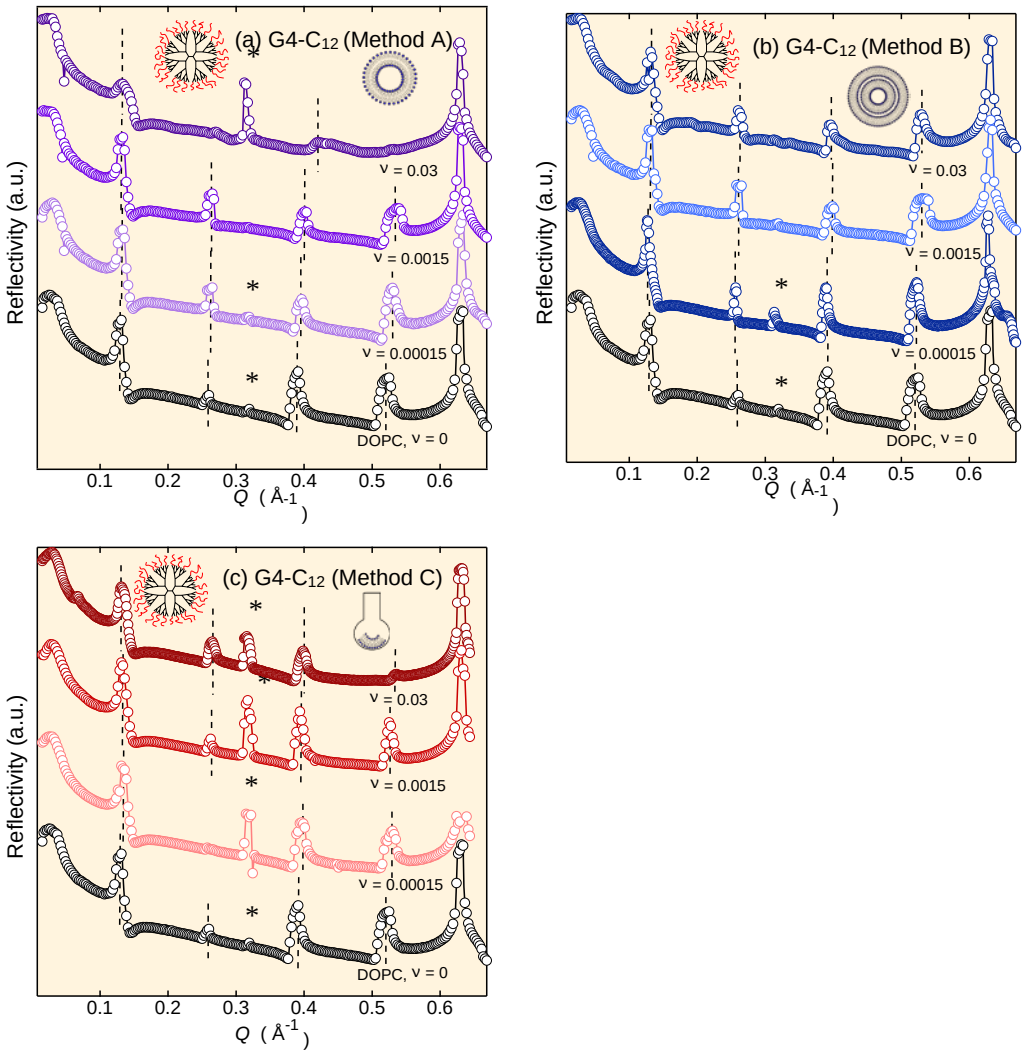

Figure S4. Reflectivity profiles of DOPC-G4-C_{12}(ν) multilayers at three number ratios (0.03, 0.0015 and 0.00015) made using mixing methods method A(a), B(b) and C(c)

S11. Scherrer analysis data tables for DOPC-G2-C_{12}(ν) and DOPC-G4-C_{12}(ν) multilayers

Table S5. *d*-spacing values for all sub-peaks *n* within Bragg peaks *h* for all three dendrimer addition methods and three dendrimer-lipid number ratios, ν for both G2 and G4 50 % C_{12} dendrimers. Error in *d*-spacing is 0.1 Å.

		d-spacing (Å) (±0.1 Å)																	
		Method A						Method B						Method C					
		G4-C_{12}			G2-C_{12}			G4-C_{12}			G2-C_{12}			G4-C_{12}			G2-C_{12}		
h	n	*0.00015*	*0.0015*	*0.03*	*0.00063*	*0.0063*	*0.127*	*0.00015*	*0.0015*	*0.03*	*0.00063*	*0.0063*	*0.127*	*0.00015*	*0.0015*	*0.03*	*0.00063*	*0.0063*	*0.127*
	0	48.3	48.4	51.6	49.2	49	46.4	49.5	49	49.7	48.8	50.7	47.6	50	47.5	48.1	48.3	47.6	43.3
1	1	46.7	46.8	47.5	47.5	48.2	44.7	49.3	47.4	47.9	48.4	48.8	46.5	47.6	47.7	47.2	46.6	45.7	42.6
	2	--	--	44	--	--	44.6	50.1	--	--	--	47.9	--	46.2	--	--	--	--	--
	0	48.6	48.1	46.4	49.2	48.9	46.4	49.3	48.6	48.5	49.5	49.2	48.2	48.7	48	47.5	48.2	47.7	43.1
2	1	47.6	47.3	44.6	48.4	48.4	45.3	48.9	47.6	48.2	48.6	48.8	47.5	--	--	--	47.2	46.7	--
	2	--	--	--	--	--	43.1	--	--	47.5	--	--	47	--	--	--	--	--	--
	0	48.3	47.3	44.9	49	48.3	45.4	49	47.7	47.2	48.7	48.6	47.3	47.6	47.9	47.3	47.7	47.5	43.6
3	1	47.6	46.8	43.3	48.4	48	44.9	48.6	47.1	47.8	47.6	47.9	47.1	--	47.6	47.3	47.9	46.7	43.4
	2	--	--	41	--	--	44.9	48.4	46.8	46.3	--	--	46.3	--	--	--	--	--	--
	0	47.6	47.5	47.8	48.5	48.3	45.5	48.4	47.5	47.5	48.6	48.4	47.5	48.3	47.8	47	48	47.3	43.5
4	1	47.3	46.6	47.2	48.2	47.7	45	48.1	46.7	46.9	47.6	47.6	47	47.5	47.8	--	47.6	46.7	43.4
	2	--	--	--	48	--	--	47.9	--	46.3	--	--	46.4	--	--	--	--	--	--
Mean		47.8	47.4	45.8	48.5	48.4	45.1	48.9	47.6	47.6	48.5	48.7	47.1	48.0	47.8	47.4	47.7	47.0	43.3
Std Error		0.2	0.2	0.9	0.2	0.1	0.3	0.2	0.2	0.3	0.2	0.3	0.2	0.4	0.1	0.1	0.2	0.2	0.1

Table S6. Coherence length, L_s, values for all sub-peaks *n* within Bragg peaks *h* for Methods A and B and three dendrimer-lipid number ratios, v for both G2 and G4 50 % C_{12} dendrimers calculated using Scherrer analysis. Errors are sometimes large due to small number of points in peaks, resulting in larger errors in peak fitting and FWHM values.

		L_s (Å)											
		Method A						Method B					
		G4-C_{12}			G2-C_{12}			G4-C_{12}			G2-C_{12}		
h	n	*0.00015*	*0.0015*	*0.03*	*0.00063*	*0.0063*	*0.127*	*0.00015*	*0.0015*	*0.03*	*0.00063*	*0.0063*	*0.127*
1	0	1170±10	1150±50	190±70	1220±10	990±40	1100±100	4900±200	1820±10	2500±100	1150±40	2360±30	900±100
	1	1820±40	2000±300	500±10	2080±10	2200±700	1500±100	2370±30	2790±10	2500±100	--	2190±10	2100±400
	2	--	--	820±60	--	--	--	5700±360	--	--	--	1560±10	--
2	0	1410±10	1180±10	760±80	1600±500	1200±10	920±70	6300±900	1930±30	400±50	1820±10	2330±40	2100±500
	1	1900±10	2600±1400	390±130	1800±400	2240±10	1460±60	3250±30	2220±60	1600±300	1450±10	1630±10	--
	2	--	--	--	--	--	700±200	--	--	1500±600	--	--	2100±300
3	0	1400±400	910±50	520±30	--	890±10	1240±40	--	810±10	1300±300	1240±30	1500±60	1000±600
	1	1000±60	1720±60	230±30	1200±200	1730±10	1620±50	1800±600	1800±100	1010±40	1200±500	700±300	--
	2	--	--	210±80	--	--	320±40	2400±200	400±200	300±100	--	--	1200±400
4	0	730±50	400±200	2360±10	940±30	590±60	1000±200	800±90	410±20	760±50	1190±10	1210±20	1300±500
	1	1600±900	500±200	1090±10	1040±120	1110±60	1200±90	1570±250	1330±150	--	1100±600	850±240	1100±100
	2	--	--	--	460±340	--	--	3400±1500	--	250±420	--	--	690±590

Table S7. Coherence length values for all sub-peaks *n* within Bragg peaks *h* for Method C and three dendrimer-lipid number ratios, v for both G2 and G4 50 % C_{12} dendrimers calculated using Scherrer analysis. * Errors are large due to small number of points in peaks, resulting in larger errors in peak fitting and FWHM values.

		L_s (Å) Method C					
		G4-C_{12}			G2-C_{12}		
h	n	*0.00015*	*0.0015*	*0.03*	*0.00063*	*0.0063*	*0.127*
1	0	3100±100	710±40	1800±100	1580±20	1320±20	970±80
	1	2000±100	1190±10	860±20	1920±60	1650±40	1700±300
	2	1320±30	--	--	--	--	--
2	0	2100±120	1600±200	810±20	1490±10	1570±90	1470±60
	1	--	--	--	1700±50	1240±60	--
3	0	650±30	1500±100	680±20	1500±700	1400±100	860±30
	1	--	1000±200	2900±700	850±50	1000±50	--
	2	--	--	--	--	--	--
4	0	1400±200	630±20	730±80	700±400	1000±200	1320±10
	1	700±30	1470±30	--	1200±140	1100±200	1900±10

Table S8. Number of layers, *m* for all sub-peaks *n* within Bragg peaks *h* for G2 and G4 -C_{12} dendrimers at three number ratios. Largest contribution in error was from FWHM used to calculate coherence length.

		number of layers, *m*																	
		Method A						Method B						Method C					
		G4-C_{12}			G2-C_{12}			G4-C_{12}			G2-C_{12}			G4-C_{12}			G2-C_{12}		
h	n	*0.00015*	*0.0015*	*0.03*	*0.00063*	*0.0063*	*0.127*	*0.00015*	*0.0015*	*0.03*	*0.00063*	*0.0063*	*0.127*	*0.00015*	*0.0015*	*0.03*	*0.00063*	*0.0063*	*0.127*
	0	24±1	24±1	4±1	25±1	20±1	24±2	99±4	37±1	51±1	24±1	47±1	19±2	62±2	15±1	37±2	33±1	28±1	22±2
1	1	39±1	43±6	11±1	44±	50±20	34±2	48±1	59±1	53±1	--	45±1	45±1	42±2	2±1	18±1	41±1	36±1	40±7
	2	--	--	19±	--	--	--	114±7	--	--	--	32±1	--	29±1	--	--	--	--	--
	0	29±1	25±1	16±2	30±10	25±1	20±2	130±20	40±1	8±1	37±1	47±1	40±10	43±2	33±4	17±1	31±1	33±2	34±1
2	1	40±1	60±30	9±3	37±8	46±1	32±1	66±1	47±1	33±6	30±1	33±1	--	--	--	--	36±1	27±1	--
	2	--	--	--	--	--	16±5	--	--	30±10	--	--	45±6	--	--	--	--	--	--
	0	29±8	19±1	12±1	--	18±1	27±1	--	17±1	28±6	25±1	31±1	20±10	14±1	31±2	14±1	30±20	29±2	20±1
3	1	21±1	37±1	5±1	25±4	36±1	36±1	40±10	38±2	21±1	30±10	15±6	--	--	21±4	60±20	18±1	21±1	--
	2	--	--	5±2	--	--	7±1	50±4	9±4	6±2	--	--	26±9	--	--	--	--	--	--
	0	15±1	8±4	49±1	19±1	12±1	22±4	17±2	9±1	16±1	24±1	25±1	30±10	29±4	13±1	16±2	15±8	21±4	30±1
4	1	30±20	11±4	23±1	22±2	23±1	27±2	33±5	28±3	--	20±10	18±5	23±2	15±1	31±1	--	25±3	24±4	44±1
	2	--	--	--	10±7	--	--	70±30	--	5±9	--	--	20±10	--	--	--	--	--	--

S12. DOPC-G4-C_{12}(ν) multilayers peak broadening analysis

Peak broadening analysis was possible for some samples but often had large associated errors. For this reason, any change in L_b with number ratio or dendrimer termination is mostly within error bounds. DOPC-G4-C_{12} multilayers mixed using Method C are an exception to this which show a distinct decrease in L_b with increasing ν. Between DOPC-G4-C_{12}(0.00015) and DOPC-G4-C_{12}(0.0015) there is a decrease in L_b from 1500±400 Å to 850±10 Å and a further decrease to 610±10 Å for DOPC-G4-C_{12}(0.03), corresponding to an overall decrease ΔL_b of ~900 Å between the lowest and highest G4-C_{12} concentration. Despite differences in the magnitude of L_b and L_s, a similar trend in an overall reduction of coherence length with ν was observed for both indicating a decrease in structural order due to the presence of an increasing number of G4-C_{12} dendrimers.

S13. XRR curves of DOPC-G4-NH_2(ν) and DOPC-G2-NH_2(ν) multilayers

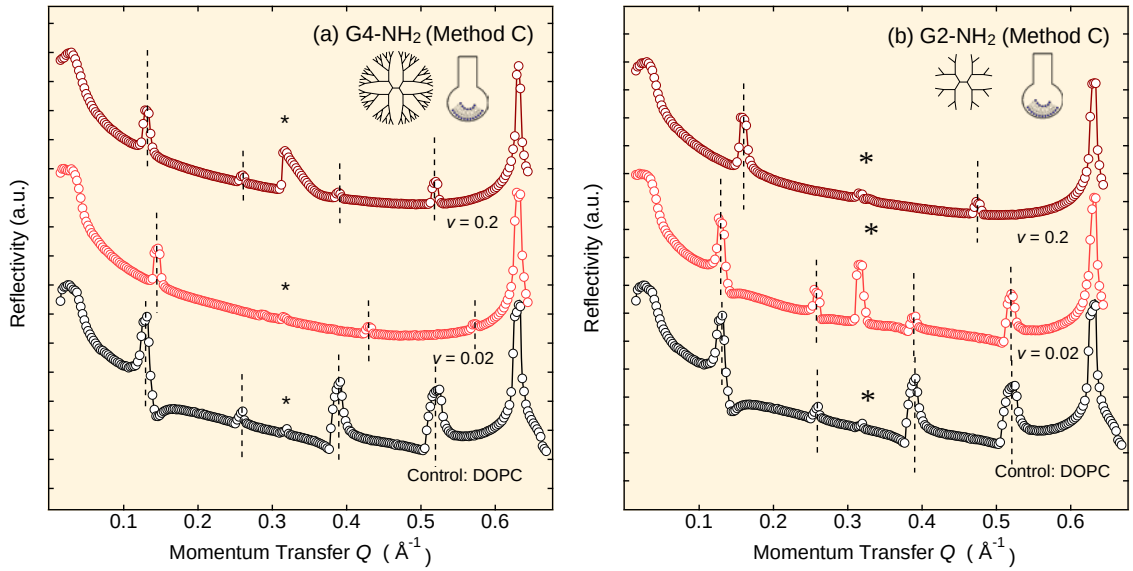

Figure S5. Reflectivity profiles for (a) DOPC-G4-NH_2 and (b) DOPC-G2-NH_2 multilayers made by incorporating dendrimers into DOPC lipid films (Method C) at number ratios ν = 0.02 and 0.002 before drop-casting. Loss of intensity of Bragg peaks indicated loss of structural order with addition of dendrimers, peak positions of multilayers containing NH_2 dendrimers shift to higher Q values, compared to DOPC-SUV, indicating bilayer thinning.

S14. Data table for DOPC-G4-NH_2(*ν*) and DOPC-G2-NH_2(*ν*) multilayers

Table S9. *d*-spacing, coherence length, L_s and number of layers, *m* for all sub-peaks ***n*** within Bragg peaks *h* for G2 and G4 NH_2 dendrimers at two number ratios. Errors in coherence length are large due to small number of points in some peaks, resulting in larger errors in fitting and hence FWHM. Error in *d*-spacing is less than 0.1 Å, standard error on the mean is given for average *d*-spacing.

		Method C											
		d-spacing (Å) ±<0.1				L_s (Å)				*m*			
		G4-NH_2		G2-NH_2		G4-NH_2		G2-NH_2		G4-NH_2		G2-NH_2	
h	*n*	*0.02*	*0.2*	*0.02*	*0.2*	*0.02*	*0.2*	*0.02*	*0.2*	*0.02*	*0.2*	*0.02*	*0.2*
1	0	44.1	48.0	49.4	40.0	2000±70	890±30	1920±30	1840±20	45±2	19±1	39±1	46±1
	1	42.8	--	47.8	38.9	1530±30	--	1600±100	1430±30	36±1	--	33±2	37±1
2	0	43.5	48.3	48.9	--	700±100	980±70	850±70	--	16±2	20±1	17±1	--
3	0	43.8	48.4	48.4	39.9	790±80	950±70	770±80	--	18±2	20±1	16±2	--
	1	--	--	--	39.6	--	--	--	1170±150	--	--	--	30±4
4	0	43.9	48.4	48.3	--	860±20	830±70	980±20	--	20±5	17±1	20±1	--
	1	--	--	48.7	--	--	--	1680±80	--	--	--	34±2	--
Mean		43.6	48.3	48.6	39.6								
Std Error		0.2	0.1	0.2	0.2								

S15. *d*-spacing and coherence length (L_s) plots for DOPC-G4-NH_2(ν) and DOPC-G2-NH_2(ν) multilayers

d-spacing and coherence length, L_s, values as a function of dendrimer-to-lipid number ratio, ν, for DOPC-G2-NH_2 and DOPC-G4-NH_2 multilayers are shown in Figure S6 and Figure S7 respectively. L_s of DOPC-Gi-NH_2C multilayers was also analysed (red circles; Figure S7). Overall, it was smaller than the control DOPC-SUV multilayers (dotted line; Figure S7) and decreased with increasing ν. Since only two ν values of NH_2 dendrimers were studied it is not possible to confirm if there was an overall trend. However, from the data points obtained, L_s was found to be smallest at the highest ν. This indicated that the presence of NH_2 terminated dendrimers caused increased disorder in the lipid multilayer structure. There was also a larger decrease in L_s for the multilayers containing G4-NH_2 dendrimers compared to G2-NH_2. Interestingly, for DOPC-G4-NH_2C multilayers, no significant change in the *d*-spacing was observed at high ν, (*cf*. Figure S6a) but there was a decrease in L_s (*cf*. Figure S7). This could indicate the presence of dendrimers at crystallite boundaries resulting in a reduction in crystallite size but no significant effect on lamellar *d*-spacing.

DOPC-G4-NH_2(0.02)C h = 2-4 Bragg peaks yielded significantly smaller L_s values (L_s ~700-860 Å) than h = 1 peaks (L_s ~2000 and ~1500 Å). This could be due to the co-existence of the ordered pure DOPC multilayers (Table S9). For DOPC-G4-NH_2(0.2)C, disappearance of the narrower Bragg peaks could indicate a more even distribution of G4-NH_2 dendrimers at the crystallite boundaries throughout the sample, leading to smaller L_s.

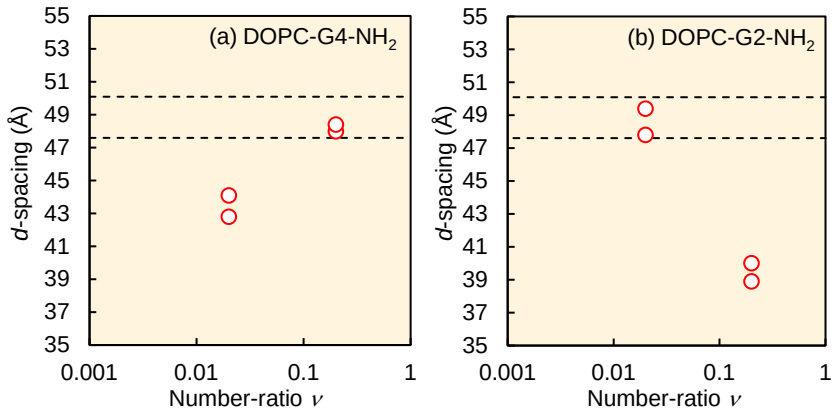

Figure S6. *d*-spacing upper and lower bounds of (a) DOPC-G4-NH_2(ν) and (b) DOPC-G2-NH_2(ν). Dotted lines indicate *d*-spacing range for pure DOPC multilayers. Dendrimers were added to DOPC lipid films (Method C) before drop-casting. Error δd = ± 0.1 Å.

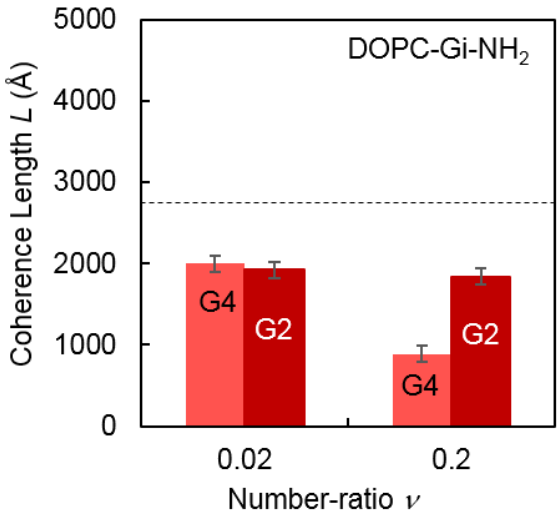

Figure S7. Coherence length L_s calculated using the Scherrer analysis from the first peak resolved from the h = 1 Bragg peak (1,0) for DOPC-G2-NH_2 and DOPC-G4-NH_2 at two number ratios ν. Dotted line indicates the coherence length for pure DOPC (1,0) multilayers, for which the error δL varies with fitting of FWHM and in all cases is < 10%.

S16. Dendrimer aggregates

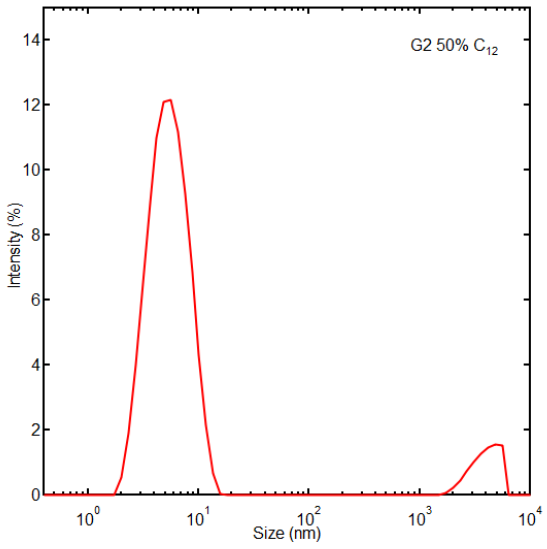

Figure S8. DLS data for a dispersion of G2 50% C_{12} dendrimer in Milli-Q water showing the presence of individual dendrimers (~3 nm) as well as large aggregates (~ 2 -6.5 μm).

S17. Multilayer fitting

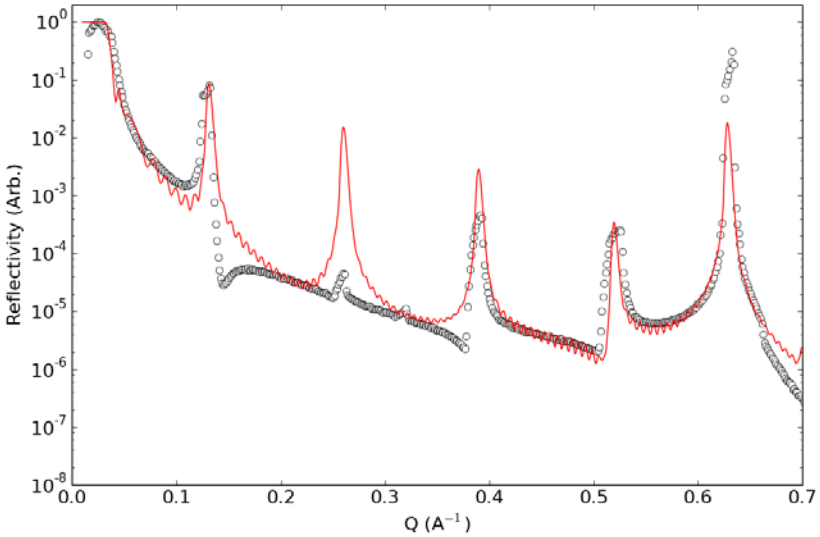

Figure S9. Fitting of DOPC multilayers using a stacked multilayer model with one domain and 36 layers, and the fitted average d-spacing is 48.4 Å. Black circles represented experimental data and the solid red line is the fit. The drop cast films are non-uniform across the footprint of the XRR measurement, with large surface roughness and the presence of several polymorphs.

References

1. Sironi, B., et al., *Structure of lipid multilayers via drop casting of aqueous liposome dispersions.* Soft Matter, 2016. **12**(17): p. 3877-87.
2. Akesson, A., et al., *The effect of PAMAM G6 dendrimers on the structure of lipid vesicles.* Phys Chem Chem Phys, 2010. **12**(38): p. 12267-72.
3. Tiriveedhi, V., et al., *Kinetic analysis of the interaction between poly(amidoamine) dendrimers and model lipid membranes.* Biochim Biophys Acta, 2011. **1808**(1): p. 209-18.
4. Zhang, Z.Y. and B.D. Smith, *High-generation polycationic dendrimers are unusually effective at disrupting anionic vesicles: Membrane bending model.* Bioconjugate Chem, 2000. **11**(6): p. 805-814.
5. Caminiti, R., et al., *Effect of hydration on the long-range order of lipid multilayers investigated by in situ time-resolved energy dispersive X-ray diffraction.* Chemical Physics Letters, 2005. **409**(4-6): p. 331-336.
6. Li, J., et al., *Visualization and Characterization of Poly(amidoamine) Dendrimers by Atomic Force Microscopy.* Langmuir, 2000. **16**(13): p. 5613-5616.

a